

On the numerical behavior of diffuse-interface methods for transcritical real-fluids simulations

Peter C. Ma*, Hao Wu, Daniel T. Banuti, Matthias Ihme

Department of Mechanical Engineering, Stanford University, Stanford, CA, 94305, USA



ARTICLE INFO

Article history:

Received 28 January 2018

Revised 25 January 2019

Accepted 31 January 2019

Available online 2 February 2019

Keywords:

Diffuse-interface methods

Quasi-conservative schemes

Transcritical flows

Real fluids

ABSTRACT

Accurate and robust simulations of transcritical real-fluid flows are crucial for many engineering applications. Diffuse-interface methods are frequently employed and several numerical schemes have been developed for simulating transcritical flows. These schemes can be categorized into two types, namely fully conservative (FC) and quasi-conservative (QC) schemes. In this study, numerical analysis is conducted to show that the mixing processes for isobaric systems follow the limiting cases of adiabatic and isochoric mixing models when FC and QC schemes are employed, respectively. It is shown that these distinct mixing behaviors are a consequence of numerical diffusion instead of physical diffusion, and can be attributed to insufficient spatial resolution. By considering several test cases, numerical simulations confirm these theoretical results. The analysis of experimental data suggests that the isochoric mixing provides better agreement in terms of the phase separation behavior. This analysis provides quantitative understanding on the interpretation of numerical simulation results and the mixing models that are commonly used to study transcritical flows.

© 2019 Elsevier Ltd. All rights reserved.

1. Introduction

The injection of fuel at transcritical conditions is widely used in diesel engines, gas turbines, and rocket motors (Mayer et al., 2000; Oswald et al., 2006; Chehroudi, 2012; Oefelein et al., 2012). A schematic of the transcritical injection process is provided in Fig. 1. In accordance with pure fluid behavior, it has been assumed traditionally that fluids at supercritical pressures do not break up into droplets upon injection, but disintegrate through a turbulent mixing process (Oswald et al., 2006; Newman and Brzustowski, 1971; Mayer and Tamura, 1996; Candel et al., 2006). However, from a thermodynamical point of view, the critical pressure of the mixture may significantly exceed the critical pressures of the pure components (Poling et al., 2001; Elliott and Lira, 2012). Consequently, at a chamber pressure that is nominally supercritical with respect to the pure propellants, the local mixture may experience a subcritical pressure, allowing for phase separation (Poling et al., 2001; Habiballah et al., 2006; Dahms and Oefelein, 2015). This has been observed experimentally for different fluid mixtures (Mayer et al., 1998; Roy et al., 2013; Manin et al., 2014). However, determining whether or not phase separation may occur under typical transcritical conditions and the importance of interfaces and sur-

face tension forces at these high pressure conditions remain open questions (Yang, 2000; Bellan, 2000; Dahms et al., 2013; Banuti et al., 2017).

To study transcritical flows numerically, diffuse-interface methods have been used, and different numerical schemes have been adopted. Table 1 provides a survey of compressible solvers that have been developed and employed by different groups for calculating these flows. In these solvers, the surface tension force is typically not considered, and the corresponding states principle (Ely and Hanley, 1981, 1983) is adopted with a pure fluid assumption for mixtures. Traditionally, fully conservative (FC) schemes have been used for transcritical flows. However, several groups have reported numerical difficulties or even failures with FC schemes in conjunction with a real-fluid state equation, due to the occurrence of spurious pressure oscillations (Schmitt et al., 2010; Matheis and Hickel, 2018; Hickey et al., 2013; Lacaze et al., 2017). This has motivated the development of quasi-conservative (QC) schemes for transcritical flows. Schmitt et al. (2010) and Ruiz (2012) added a correction term in the energy equation by connecting artificial dissipation terms in the mass, momentum, and energy conservation equations, and setting the pressure differential to zero. Since the correction term is not in flux form, the scheme is not strictly energy-conserving. Inspired by the pioneering work of Karni (1994) and Abgrall (1996) for ideal-gas multi-component flows, Terashima and Koshi (2012) and Kawai et al. (2015) solved a transport equation for pressure instead of the total energy equation

* Corresponding author.

E-mail address: peterma@stanford.edu (P.C. Ma).

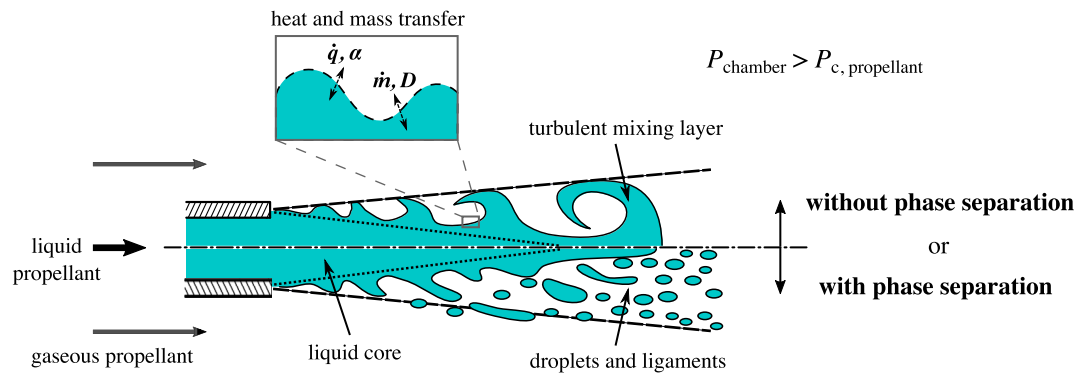


Fig. 1. Schematic of transcritical injection process with (bottom) and without (top) phase separation. The interfacial thermodynamic state depends on the local temperature and composition, which is determined by diffusion of heat and mass, \dot{q} and \dot{m} , respectively.

Table 1

Representative numerical solvers used by different groups for compressible transcritical flow simulations using diffuse-interface methods.

Group (Solver)	Spatial discretization ^a	Temporal discretization	Special treatment	FC/QC ^b	EoS ^c
JPL (Miller and Bellan, 1999; Miller et al., 2001; Okong'o and Bellan, 2002)	Finite difference, eighth-order central difference	Explicit RK4	–	FC	PR
Georgia Tech (Meng and Yang, 2003; Zong and Yang, 2008; Wang et al., 2017)	Fourth-order central difference with artificial viscosity	Dual-time stepping with second-order backward difference	–	FC	SRK
Sandia (RAPTOR) (Lacaze and Oefelein, 2013; Lacaze et al., 2015; Ruiz et al., 2016)	Third-order QUICK and first-order upwind switching with flux limiter	Dual-time stepping with second-order backward difference	–	FC	PR
CERFACS (AVBP) (Ruiz et al., 2016; Schmitt et al., 2010; Ruiz, 2012)	Third-order TTGC with artificial viscosity	Explicit RK3	Non-conservative energy correction term	QC	PR
Terashima and Kawai (Terashima and Koshi, 2012; Kawai et al., 2015)	Finite difference, sixth-order Pade with LAD	Explicit RK3	Pressure evolution equation	QC	PR
TUM (INCA) (Müller et al., 2016; Matheis and Hickel, 2016, 2018)	ALDM	Explicit RK3	–	FC	PR with VLE for mixtures
CNRS (SiTCom-B) (Petit et al., 2013, 2015)	Fourth-order skew-symmetric-like scheme with artificial viscosity	Explicit RK4	–	FC	PR, SRK
BOSCH (CharLES) (Knudsen et al., 2017)	Hybrid central-ENO with sensor	Explicit RK3	–	FC	PR with modified Psat
Pantano et al. (Pantano et al., 2017)	First-order with Riemann solver	First-order Euler explicit	Extra transport equation	QC	vdW
Stanford (CharLES*) (Ma et al., 2017)	Hybrid central-ENO with sensor, entropy-stable	Explicit RK3	Double-flux model	QC	PR

^a Finite volume scheme is considered unless otherwise stated.

^b FC = fully conservative scheme, QC = quasi conservative scheme

^c EoS = equation of state, SRK = Soave-Redlich-Kwong, PR = Peng-Robinson, vdW = van der Waals, VLE = vapor liquid equilibrium, Psat = saturation pressure

in their finite difference solver so that the pressure equilibrium across contact interfaces is maintained. Pantano et al. (2017) formulated a numerical scheme for transcritical contact and shock problems, which introduces an additional non-conservative transport equation for maintaining the mechanical equilibrium of pressure. Ma et al. (2014, 2017) extended a double-flux model (Abgrall and Karni, 2001; Billet and Abgrall, 2003) to the transcritical regime, which is capable of eliminating spurious pressure oscillations. Hybrid schemes that combine FC and QC schemes have also been developed in the context of shock-dominated flows (Karni, 1996; Lee et al., 2013). These hybrid schemes address the limitation of QC schemes in correctly predicting the shock speed (Abgrall and Karni, 2001); however, such developments are currently limited for transcritical flows. Apart from single-fluid models, other

approaches for phase transitions have been proposed. In these approaches, the Navier-Stokes-Korteweg equations are solved to represent two-phase flows (Gomez et al., 2010; Tian et al., 2016).

Discrepancies in the mixing behaviors between FC and QC schemes have been reported in the literature. The solver AVBP with a QC scheme and the FC solver RAPTOR were both used to simulate a benchmark test case of a LOX/GH2 mixing layer (Ruiz et al., 2016). Despite similar behaviors for axial and transverse velocity profiles and species mass fractions, significant differences in both the mean and root-mean-square (rms) values of the temperature field were observed. The origin of these differences were not investigated. Large-eddy simulations (LES) of the ECN Spray A case (Pickett and Bruneaux, 2011) were performed by Matheis and Hickel (2016), and the temperature field

was found to be significantly higher when using a QC scheme. This discrepancy was attributed to the energy conservation error. Lacaze et al. (2017) pointed out that the adiabatic mixing profile can be obtained only by using a FC scheme. To fully understand the impact of numerical methods on the mixing behaviors, a systematic analysis is required. This issue is addressed in this work.

The adiabatic mixing process has been considered in several previous studies to describe transcritical flows. For numerical simulations, Lacaze et al. (2015) compared their simulation results with the adiabatic mixing and attributed the slight deviations of the solutions from adiabatic mixing to transport anomalies. Through theoretical analysis, Dahms and Oefelein (2015) and Dahms et al. (2013) approached the problem using linear gradient theory in conjunction with the adiabatic mixing assumption. Qiu and Reitz (2015) and Qiu et al. (2014) examined the thermodynamic stability of the local mixture, accounting for a subsequent reduction in temperature when phase separation occurs. Experimentally, the ECN workshop (Pickett and Bruneaux, 2011) has been using the adiabatic mixing model to relate mixture fraction measurements to temperature in order to enable a validation of numerical simulations.

However, several studies have been performed in which diffusion of heat and mass are treated individually without imposing additional assumptions. The thermodynamic behavior of isolated transcritical droplets in gaseous environments has been studied computationally (Delplanque and Sirignano, 1993; Yang et al., 1994; Haldenwang et al., 1996; Harstad and Bellan, 1998; Sirignano and Delplanque, 1999; Harstad and Bellan, 2000), typically relying on a transition from a sharp to a diffuse-interface when the mixture critical temperature is locally exceeded. Instead, by analyzing the local thermodynamic state of hydrogen-oxygen diffusion flames, it was found that reactive cases are more susceptible to phase separation than inert mixing (Banuti et al., 2018; Lacaze and Oefelein, 2012). This can be attributed to the fact that the combustion product water significantly reduces the local critical pressure of the mixture. The Y - T mixing lines, shown by Harstad and Bellan (1998), deviate qualitatively from the adiabatic mixing line, which stands in contrast to the simultaneous change in both mole fraction and temperature observed during adiabatic mixing. Harstad and Bellan (1999) attributed this to an effective Lewis number in the case of transcritical evaporation, while adiabatic mixing corresponds to a unity Lewis number assumption.

The objective of this study is to investigate the representation of mixing processes at transcritical conditions from different schemes through numerical analysis and simulations. Governing equations, thermodynamic relations, and numerical schemes considered are presented in Section 2. In Section 3, the two limits of adiabatic and isochoric mixing are introduced and analyzed. Physical explanations for the distinctly different mixing behaviors are provided through theoretical analysis of the numerical diffusion processes. These theoretical findings are confirmed through numerical simulations. Results for typical transcritical injection conditions using both FC and QC schemes are presented in Section 4, and the mixing behaviors are assessed utilizing the analytical results from Section 3. These numerical results are connected to practical applications by examining measurements to identify experimentally observed mixing behaviors. The manuscript finishes with conclusions in Section 5.

2. Mathematical formulation

2.1. Governing equations

The governing equations for the diffuse-interface method considered in this study are the conservation of mass, momentum,

total energy, and species, taking the following form

$$\frac{\partial \rho}{\partial t} + \nabla \cdot (\rho \mathbf{u}) = 0, \quad (1a)$$

$$\frac{\partial (\rho \mathbf{u})}{\partial t} + \nabla \cdot (\rho \mathbf{u} \mathbf{u} + \mathbf{p} \mathbf{I}) = \nabla \cdot \boldsymbol{\tau}, \quad (1b)$$

$$\frac{\partial (\rho E)}{\partial t} + \nabla \cdot [\mathbf{u}(\rho E + p)] = \nabla \cdot (\boldsymbol{\tau} \cdot \mathbf{u}) - \nabla \cdot \mathbf{q}, \quad (1c)$$

$$\frac{\partial (\rho Y_k)}{\partial t} + \nabla \cdot (\rho \mathbf{u} Y_k) = \nabla \cdot (\rho D_k \nabla Y_k) \quad \text{for } k = 1, \dots, N_S - 1, \quad (1d)$$

where ρ is the density, \mathbf{u} is the velocity vector, p is the pressure, E is the specific total energy, Y_k is the mass fraction of species k , D_k is the diffusion coefficient for species k , and N_S is the number of species. The viscous stress tensor and heat flux are written as

$$\boldsymbol{\tau} = \mu [\nabla \mathbf{u} + (\nabla \mathbf{u})^T] - \frac{2}{3} \mu (\nabla \cdot \mathbf{u}) \mathbf{I}, \quad (2a)$$

$$\mathbf{q} = -\lambda \nabla T - \rho \sum_{k=1}^{N_S} h_k D_k \nabla Y_k, \quad (2b)$$

where μ is the dynamic viscosity, λ is the thermal conductivity, T is the temperature, and h_k is the partial enthalpy of species k . The specific total energy is related to the internal energy, e , and the kinetic energy,

$$E = e + \frac{1}{2} \mathbf{u} \cdot \mathbf{u}. \quad (3)$$

The system is closed with an equation of state (EoS), which is here written in a pressure-explicit form as

$$p = f(\rho, e, \mathbf{Y}), \quad (4)$$

where $\mathbf{Y} = [Y_1, \dots, Y_{N_S}]^T$ represents the species vector. The formulation of the state equation and the evaluation of transport properties are discussed next.

2.2. Thermodynamic relations

The analysis and results in this study are not limited to a particular EoS, and are general to real-fluid transcritical flows. The Peng-Robinson (PR) cubic EoS (Poling et al., 2001; Peng and Robinson, 1976) is employed in this study due to its acceptable accuracy, computational efficiency, and prevailing use. This state equation can be written as

$$p = \frac{RT}{v - b} - \frac{a}{v^2 + 2bv - b^2}, \quad (5)$$

where R is the gas constant, $v = 1/\rho$ is the specific volume, and the parameters a and b are dependent on temperature and composition to account for effects of intermolecular forces and volume displacement. For multi-component fluids, the mixing rules due to Harstad et al. (1997) are used and procedures for evaluating thermodynamic quantities using PR-EoS can be found in our previous work (Ma et al., 2017). The thermodynamic properties of different species considered in this study are listed in Table 2.

Vapor liquid equilibrium (VLE) calculations are conducted using PR-EoS with the equal fugacity criterion (Poling et al., 2001; Elliott and Lira, 2012). The procedure was validated with experimental measurements for mixtures relevant for transcritical flows and was successfully applied to study pseudo-boiling processes for noble gas mixtures (Raju et al., 2017).

For the numerical solvers listed in Table 1, the corresponding states principle (Ely and Hanley, 1981, 1983) is typically adopted

Table 2

Thermodynamic properties (molecular weight, critical properties for temperature, pressure, density, and compressibility, and acentric factor) for different species considered in this study. FK-5-1-12 is also referred to as fluoroketone with chemical formula $\text{CF}_3\text{CF}_2\text{C}(\text{O})\text{CF}(\text{CF}_3)_2$.

Species	W [kg/kmol]	T_c [K]	p_c [MPa]	ρ_c [kg/m ³]	Z_c	ω
H ₂	2.02	33.15	1.30	31.26	0.303	-0.219
N ₂	28.0	126.2	3.40	313.3	0.289	0.0372
O ₂	32.0	154.6	5.04	436.1	0.287	0.0222
<i>n</i> -C ₁₂ H ₂₆	170.3	658.1	1.82	226.5	0.249	0.574
FK-5-1-12	316.1	441.8	1.86	639.1	0.251	0.471

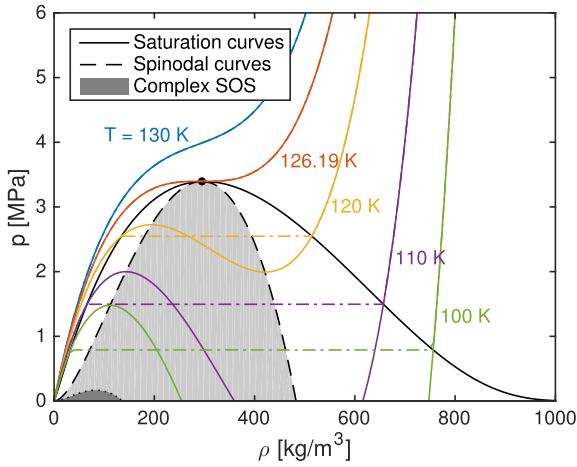


Fig. 2. p - ρ diagram for N₂ computed with PR-EoS. Black dot indicates the critical point. The unstable/non-convex thermodynamic states are enclosed by the spinodal curves. Solid lines are isotherms predicted by PR-EoS and dash-dotted lines correspond to the saturation pressure at the given temperature. Dark-gray area indicates the region of complex speed of sound (SOS).

and a pure fluid assumption is used for mixtures. For a complete EoS for a pure fluid, $e = e(v, s)$, where s is the specific entropy, the thermodynamic stability requires that e being jointly convex as a function of v and s , so that the Hessian is positive semidefinite (Saurel et al., 2008; Menikoff and Plohr, 1989; Shyue, 2001),

$$\left(\frac{\partial^2 e}{\partial s^2}\right)_v \geq 0, \quad \left(\frac{\partial^2 e}{\partial v^2}\right)_s \geq 0, \quad \left(\frac{\partial^2 e}{\partial s^2}\right)_v \left(\frac{\partial^2 e}{\partial v^2}\right)_s \geq \left(\frac{\partial^2 e}{\partial s \partial v}\right)^2. \quad (6)$$

These conditions translate to the requirements

$$c_v^{-1} \geq c_p^{-1} \geq 0, \quad \kappa_s^{-1} \geq \kappa_T^{-1} \geq 0, \quad (7)$$

where c_v and c_p are the specific heat capacities at constant volume and pressure, respectively, and κ_s and κ_T are the isentropic and isothermal compressibilities, respectively. The requirement $(\partial^2 e / \partial v^2)_s \geq 0$ implies a real-valued speed of sound, or equivalently, the hyperbolicity of the corresponding Euler system of Eq. (1).

For a typical real-fluid EoS, the criteria in Eq. (6) are satisfied outside the vapor dome. Inside the vapor dome, the thermodynamic state described by the EoS is either metastable or unstable/non-convex. Indeed, most of the EoS's, such as PR-EoS, are designed to be used outside the vapor dome. As an example, we consider the thermodynamics of pure N₂, shown in a p - ρ diagram in Fig. 2. The unstable/non-convex region is enclosed by the spinodal curves which are the loci of $(\partial p / \partial v)_T = 0$. Inside this region, negative values of c_p can be obtained by the PR-EoS. Under more severe conditions, the computed speed of sound (SOS) becomes complex-valued as can be seen in Fig. 2, but this region

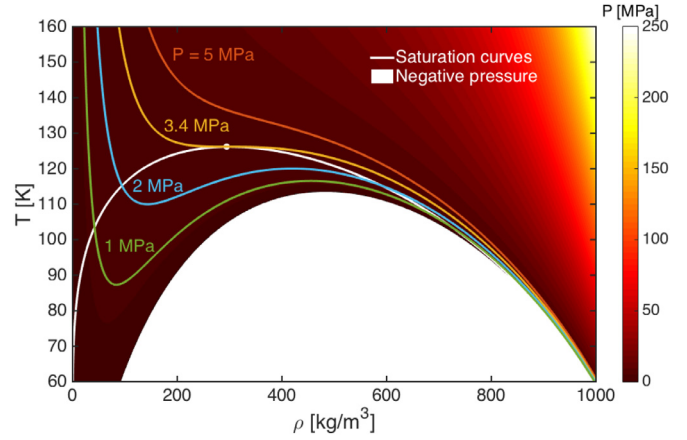


Fig. 3. T - ρ diagram for N₂ computed with PR-EoS showing pressure contours. White dot indicates the critical point. Note the large region with valid temperature and density but a negative pressure, which is shown in white.

should rarely be accessed for transcritical flow simulations at pressures corresponding to supercritical conditions.

A more disconcerting feature of typical cubic EoS's inside the vapor dome, however, is that when the temperature is relatively low, the cubic nature of the EoS yields negative pressures for certain density values. This is illustrated in Fig. 3, where pressure contours of N₂ are plotted in a T - ρ diagram. As can be seen in this figure, there is a large region with valid temperature and density values, but negative pressure (indicated by the blank area). For most of the solvers listed in Table 1, an essential step during each time step of the simulation is to determine the pressure from temperature and density, which will be discussed in details in Section 2.4 (see Fig. 4(a)). The numerical diffusion and dispersion can possibly lead the numerical solution to a thermodynamic state that has a negative pressure, which results in the failure of the numerical simulation. This is particularly an issue for FC schemes where the pressure equilibrium cannot be maintained across the transcritical contact interfaces. In contrast, for QC schemes, spurious pressure oscillations are either mitigated or eliminated so that a positive pressure is guaranteed. Note that for the two solvers that employ a dual-time stepping scheme in Table 1, pressure is not updated from temperature and density through the state equation but instead solved as a flow variable, and thus the issue of negative pressure does not occur.

To deal with the aforementioned issue of negative pressures, the original PR-EoS is modified so that for conditions at which the thermodynamic state falls inside the vapor dome, the saturation pressure is returned instead of the one calculated from the PR-EoS. This treatment is similar to that introduced by Knudsen et al. (2017), but instead with an exact saturation pressure, which is shown by the dash-dotted lines in Fig. 2. The speed of sound and other thermodynamic variables in the vapor dome are represented by a linear profile between saturated liquid state

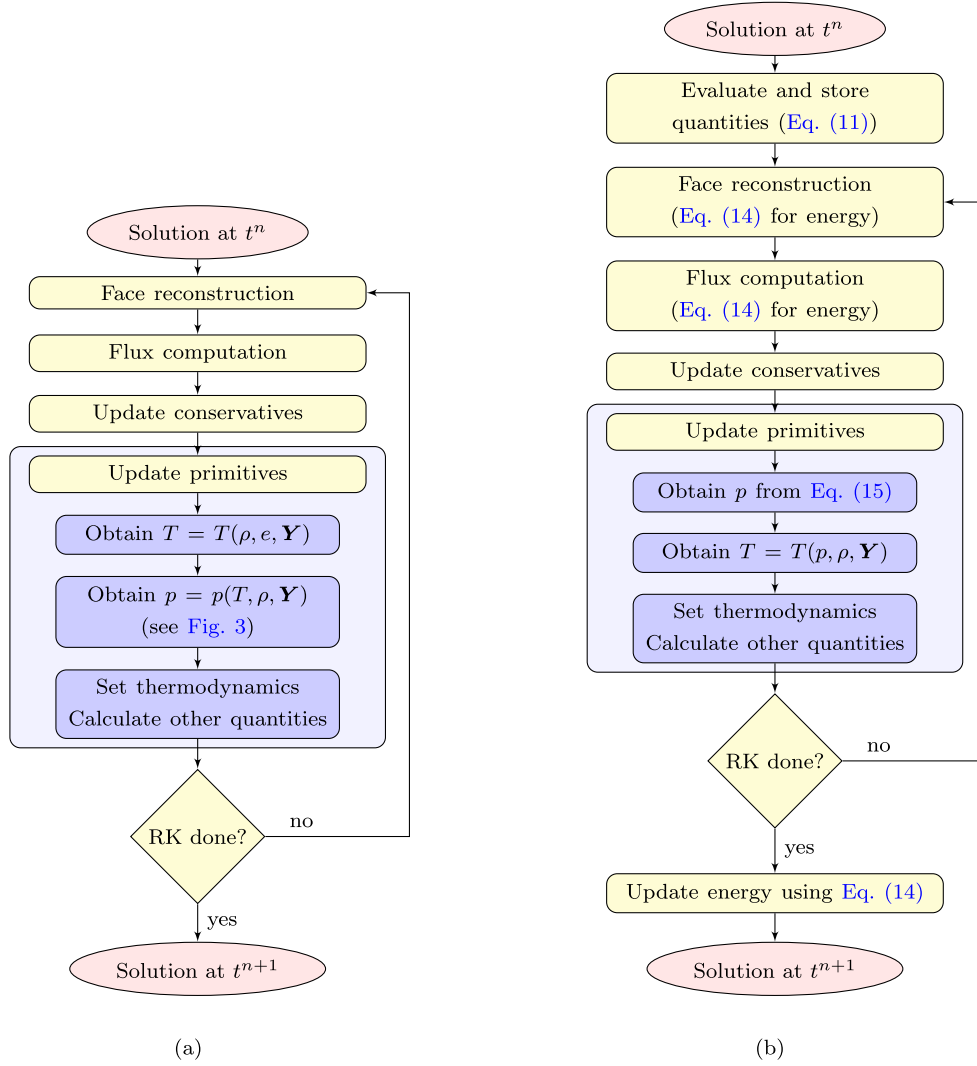


Fig. 4. Time advancement from t^n to t^{n+1} for (a) fully conservative scheme and (b) quasi-conservative scheme using the double-flux model. Only Euler flux is considered in the flowcharts. RK denotes the Runge–Kutta time integration.

and saturated vapor state, which is parameterized using the liquid volume fraction. The saturation states are evaluated from vapor-liquid equilibrium calculations. As shown in Fig. 2, using the unmodified cubic PR-EoS, the region with a complex wave speed is restricted to very low pressures. For all cases considered in this study, this region is never accessed. For the FC scheme with the modifications on the EoS, since the speed of sound is calculated based on values for saturated liquid and vapor linearly, the speed of sound is maintained to be real-valued in all of our simulations. More sophisticated formulations of the speed of sound within the two-phase region can be applied, e.g. Wood speed of sound (Wood, 1930). However, since first, regions where negative pressure could occur are expected to be localized in a supercritical environment with a constant thermodynamic pressure (e.g., see Appendix B of Ma et al., 2017), and second, the modifications made here are merely a numerical treatment to guarantee numerical robustness rather than a physical description of the wave propagation, the simple linear formulation for the speed of sound is adopted. Note that these thermodynamic treatments cannot eliminate the spurious pressure oscillations, however, they enable us to conduct transcritical flow simulations robustly with a FC scheme.

For transport properties, the dynamic viscosity and thermal conductivity are evaluated using Chung’s method with high-pressure corrections (Chung et al., 1984). This method is known to

produce oscillations for certain mixture compositions (Ruiz et al., 2016; Hickey et al., 2013). To overcome this issue, the acentric factor is set to zero only when evaluating the viscosity so that anomalies in the viscosity are removed. Takahashi’s high-pressure correction (Takahashi, 1975) is used to evaluate binary diffusion coefficients. Since only binary mixtures are considered in all test cases studied in this work, the binary diffusion coefficients are the only properties needed for the species equations and the evaluation of the diffusion coefficients is exact.

2.3. Numerical methods

A finite volume approach is utilized for the discretization of the system of equations, Eq. (1),

$$V_{cv} \frac{\partial \mathbf{U}}{\partial t} + \sum_f A_f (\mathbf{F}_f^e - \mathbf{F}_f^v) \cdot \hat{\mathbf{n}}_f = 0, \quad (8)$$

where

$$\mathbf{U} = [\rho, (\rho \mathbf{u})^T, \rho E, (\rho \mathbf{Y})^T]^T \quad (9)$$

is the vector of conserved variables, \mathbf{F}^e is the face-normal Euler flux vector, \mathbf{F}^v is the face-normal viscous flux vector, corresponding to the right-hand side (RHS) of Eq. (1), V_{cv} is the volume of

the control volume, A_f is the face area, and $\hat{\mathbf{n}}_f$ is the face normal direction.

A Strang-splitting scheme (Strang, 1968) is employed in this study to separate the convection and diffusion operators. The convective flux is discretized using a sensor-based hybrid scheme in which a high-order, non-dissipative scheme is combined with a low-order, dissipative scheme to minimize the numerical dissipation (Ma et al., 2017; Khalighi et al., 2011). For this, a central scheme, which is fourth-order on uniform meshes, is combined with a second-order ENO scheme. A density sensor (Ma et al., 2017) is adopted in this study. Due to the large density gradients at transcritical conditions, an entropy-stable flux correction technique (Ma et al., 2017) is used to ensure the physical realizability of the numerical solution and to dampen non-linear instabilities in the numerical schemes. For the discretization of the viscous flux and gradient calculations, the reader is referred to previous work by Ham and Iaccarino, 2004. A strong stability preserving 3rd-order Runge–Kutta (SSP-RK3) scheme (Gottlieb et al., 2001) is used for time integration.

2.4. Fully conservative (FC) and quasi-conservative (QC) schemes

Two different schemes are considered in this study for transcritical flow simulations, which are the FC and QC schemes. These two schemes differ from each other in the treatment of the convection operators in Eq. (1) and the procedure for evaluating the primitive variables from conservative quantities. These aspects will be discussed in the following. Algorithmic flowcharts for both schemes are provided in Fig. 4.

2.4.1. Fully conservative scheme

The detailed sequence for the time advancement from t^n to t^{n+1} for the FC scheme is shown in the flowchart of Fig. 4(a). For the FC scheme, the Euler flux at the faces of cell i is evaluated as

$$\mathbf{F}^e = \hat{\mathbf{F}}(\mathbf{U}_j) \quad \text{for } j \in \mathbf{I}_i, \quad (10)$$

where $\hat{\mathbf{F}}$ is the numerical flux, and \mathbf{I}_i denotes the spatial stencil of cell i . The evaluation of the numerical flux $\hat{\mathbf{F}}$ involves spatial reconstruction and flux calculations, and the reader is referred to Khalighi et al. (2011) for further details on this.

The conservative variables are updated using Eq. (8), after which the primitive variables are calculated using the updated conservative variables. For the FC scheme, the temperature is first calculated given the updated density, internal energy and species. For this, an iterative process is typically employed (Schmitt et al., 2010; Hickey et al., 2013). Subsequently, the pressure is evaluated from density, temperature and species. If the raw form of the PR EoS is utilized, this procedure can result in negative values of pressure, as illustrated in Fig. 3. This can lead to the failure of the numerical solver as discussed in Section 2.2. After temperature and pressure are determined, along with species information, the thermodynamic state is set, and all other thermo-transport quantities can be evaluated.

In the FC scheme, the Euler flux evaluated from the two neighboring cells of the face is exactly the same, which ensures strict conservation of the flow variables. However, due to the strong non-linearity inherent in the real-fluid EoS, spurious pressure oscillations are generated when a FC scheme is used (Terashima and Koshi, 2012; Ma et al., 2017; Lacaze et al., 2017). This issue motivated the development of QC schemes.

2.4.2. Quasi-conservative scheme

Several quasi-conservative schemes were developed for transcritical flows (Schmitt et al., 2010; Terashima and Koshi, 2012; Kawai et al., 2015; Pantano et al., 2017; Ma et al., 2017). In the present study, the double-flux model, extended for transcritical

flows (Ma et al., 2017), is selected as a representative QC scheme. The double-flux method was originally proposed by Abgrall and Karni (2001) for multi-component ideal-gas flows, and later extended to ideal-gas reacting flow systems (Billet and Abgrall, 2003) and high-order schemes (Billet and Ryan, 2011; Lv and Ihme, 2014). In this method, the relation between the pressure and the internal energy is frozen in both space and time, which converts the local system to a calorically perfect gas system. This treatment removes not only the spurious pressure oscillations but also the oscillations of other physical quantities that are induced by the pressure oscillations. Only an outline of this method is presented here and details can be found in Ma et al. (2017). The flowchart for the time advancement procedure of the QC scheme using the double-flux model is provided in Fig. 4(b). In this model, an effective specific heat ratio (or adiabatic exponent), and an effective reference energy value (Ma et al., 2017) are used to relate the pressure and the internal energy, which are defined as

$$\gamma^* = \frac{\rho c^2}{p}, \quad (11a)$$

$$e_0^* = e - \frac{pv}{\gamma^* - 1}, \quad (11b)$$

where c is the speed of sound. These two quantities are evaluated and stored as constants for each time step through all RK sub-steps.

The Euler flux at the faces of cell i is then evaluated as

$$\mathbf{F}^e = \hat{\mathbf{F}}(\mathbf{U}_j^*) \quad \text{for } j \in \mathbf{I}_i, \quad (12)$$

where

$$\mathbf{U}^* = [\rho, (\rho \mathbf{u})^T, \rho E^*, (\rho \mathbf{Y})^T]^T \quad (13)$$

with

$$(\rho E)_j^* = \frac{p_j}{\gamma_j^* - 1} + \rho_j e_{0,i}^* + \frac{1}{2} \rho_j \mathbf{u}_j \cdot \mathbf{u}_j \quad \text{for } j \in \mathbf{I}_i. \quad (14)$$

Note that in comparison to the FC scheme, the total energy is modified using Eq. (14) during the reconstruction and flux calculation steps in the double-flux model.

After the conservative variables are updated using Eq. (8), the pressure in cell i is first calculated as

$$p_i = (\gamma_i^* - 1) \left[(\rho E)_i - \rho_i e_{0,i}^* - \frac{1}{2} \rho_i \mathbf{u}_i \cdot \mathbf{u}_i \right], \quad (15)$$

given the density and total energy. The temperature is then evaluated from the pressure, density and species using the EoS. For cubic EoS's, an analytical solution can be found for the temperature (Ma et al., 2017). With temperature and pressure determined, the thermodynamic state is defined and all other thermo-transport quantities are updated subsequently. Finally, after all RK sub-steps are evaluated, the total energy is updated from the primitive variables using Eq. (14) in order to ensure the thermodynamic consistency. Note that for the QC scheme, the step in the FC scheme where the pressure is determined from density, temperature and species as shown in Fig. 3 is absent, so that the pressure remains positive.

Since different values of γ^* and e_0^* are used for each cell, the two energy fluxes at a face are no longer the same, resulting in an energy conservation error. The conservation error in total energy was shown to converge to zero with increasing resolution and reduction in the difference in γ^* between neighboring cells (Ma et al., 2017; Abgrall and Karni, 2001). Note that the double-flux method has similar performance and conservation behavior as the pressure evolution method (Terashima and Koshi, 2012; Kawai et al., 2015), which is another QC scheme that is commonly used for transcritical flows. Indeed, the two approaches are equivalent for a contact interface problem. Therefore, the numerical analysis

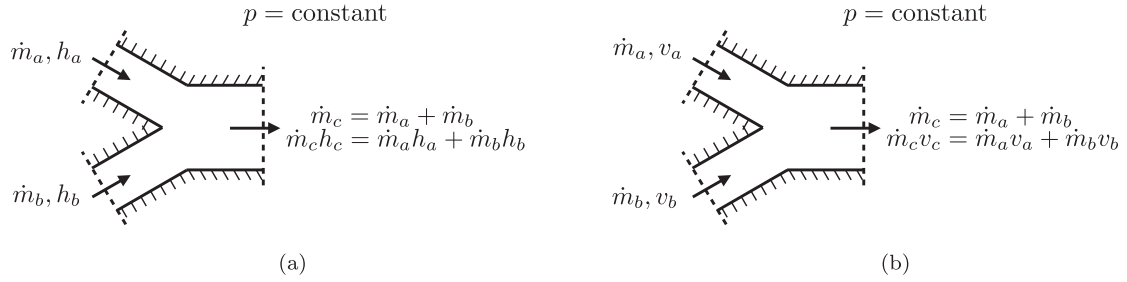


Fig. 5. Schematic of (a) isobaric-adiabatic and (b) isobaric-isochoric mixing. \dot{m} is the mass flow rate, h is the specific enthalpy, v is the specific volume, and p is the pressure.

and comparison in this study are expected to be applicable to both schemes.

Note that the numerics along with other thermo-transport models are kept identical for the FC and QC schemes considered in this study. The only exceptions are the convective flux evaluation and the way the pressure is updated, thereby facilitating a fair comparison between both schemes.

3. Analysis of numerical mixing

3.1. Adiabatic and isochoric mixing

Before the numerical analysis is conducted, two types of thermodynamic mixing processes are introduced. These mixing processes correspond to the limiting cases of isobaric-adiabatic mixing and isobaric-isochoric mixing, and are further analyzed in the following. Fig. 5 provides a schematic illustration of the physical representations of these two mixing models. For most applications that are relevant to this study, the thermodynamic pressure of the system is maintained to be constant, e.g., by the choked nozzle in rocket engines, or during the isobaric combustion phase at the top-dead-center in diesel engines. Therefore, isobaric mixing processes are considered and this assumption is employed throughout the numerical analysis in the rest of this study.

3.1.1. Adiabatic mixing

For the adiabatic mixing shown in Fig. 5(a), the two streams mix without heat exchange, so that the enthalpy is conserved. This can be represented by the following binary mixing process

$$\dot{m}_c = \dot{m}_a + \dot{m}_b, \tag{16a}$$

$$\dot{m}_c h_c = \dot{m}_a h_a + \dot{m}_b h_b, \tag{16b}$$

where \dot{m}_α is the mass flow rate of the stream α and h represents the specific enthalpy. In the following, we consider a binary mixing system and denote Y as the mass fraction of the first species. Under the condition that both streams contain pure species, i.e., $Y_a = 1$ and $Y_b = 0$, then the specific enthalpy of the mixed stream can be expressed as

$$h_c = Y_c h_a + (1 - Y_c) h_b, \tag{17}$$

with $Y_c = \dot{m}_a / (\dot{m}_a + \dot{m}_b) = \dot{m}_a / \dot{m}_c$. For a general case, if the two streams before mixing both consist of binary mixtures and with the mass conservation for the first species

$$\dot{m}_c Y_c = \dot{m}_a Y_a + \dot{m}_b Y_b, \tag{18}$$

we have

$$h_c = \frac{\dot{m}_a}{\dot{m}_c} h_a + \frac{\dot{m}_b}{\dot{m}_c} h_b = \frac{Y_c - Y_b}{Y_a - Y_b} h_a + \frac{Y_a - Y_c}{Y_a - Y_b} h_b. \tag{19}$$

From Eq. (19) it can be seen that for an adiabatic mixing process the specific enthalpy of the mixed stream is a linear function of the mixed mass fraction.

The adiabatic mixing model has been used in several studies related to transcritical flows (Dahms et al., 2013; Lacaze et al., 2015; Matheis and Hickel, 2016; 2018; Qiu and Reitz, 2015) either for the evaluation of numerical simulation results, or as an assumption for the analysis of phase separation behaviors.

3.1.2. Isochoric mixing

In contrast to the adiabatic mixing, if the two streams are mixed isochorically, as shown in Fig. 5(b), the volume of the binary mixture is conserved,

$$\dot{m}_c = \dot{m}_a + \dot{m}_b, \tag{20a}$$

$$\dot{m}_c v_c = \dot{m}_a v_a + \dot{m}_b v_b, \tag{20b}$$

and this gives a specific volume profile that is linear in the mixed mass fraction,

$$v_c = Y_c v_a + (1 - Y_c) v_b. \tag{21}$$

Similarly to the adiabatic mixing process, for the condition when both inlet streams consist of a binary mixture, we have

$$v_c = \frac{Y_c - Y_b}{Y_a - Y_b} v_a + \frac{Y_a - Y_c}{Y_a - Y_b} v_b. \tag{22}$$

This process is achieved by heat transfer between the mixture and the surrounding.

For a given constant pressure, the adiabatic mixing line in the T - X state space can be computed from Eq. (17) by converting enthalpy into the corresponding temperature. Similarly, the isochoric mixing line can be computed from Eq. (21) by calculating the temperature from specific volume using the EoS.

3.2. Resolution requirements

To examine the relevance of numerical diffusion, a discussion of the grid resolution requirement is provided in this subsection. For this, we consider the ratio of convection and diffusion time scales, which can be expressed by the Peclet number as

$$Pe_D = \frac{LU}{D} = Re Sc, \quad Pe_\alpha = \frac{LU}{\alpha} = Re Pr, \tag{23}$$

where L and U are the characteristic length and velocity, D and α are the mass and thermal diffusion coefficients, respectively; Pe_D and Pe_α are the Peclet numbers for mass and heat transfer, respectively, Re is the Reynolds number, Sc is the Schmidt number, and Pr is the Prandtl number.

Typical transcritical flows operate at high Reynolds number conditions. Furthermore, the mass diffusion coefficient for gas scales inversely with pressure, and the ratio of the diffusion coefficients between gaseous and liquid is rather small. This yields an even larger Peclet number than that typically encountered in flows at ideal-gas conditions. As an example, by considering the LOX/GH2 mixing layer case examined in Section 4.2, the characteristic length scale, which is the injector lip height, is 0.5 mm,

and the characteristic velocity is 40 m/s (Ruiz et al., 2016), the mass diffusivity of an equimolar H₂ and O₂ mixture at 10 MPa and 100 K is about 2×10^{-8} m²/s (Harstad and Bellan, 1998). This leads to a Peclet number on the order of $\mathcal{O}(10^6)$. The large molecular diffusion time scale compared to the convection time scale indicates that effects of molecular diffusion in the governing equations may be significantly reduced. This suggests that, for high Reynolds number flows, it may be infeasible for a typical mesh resolution utilized by a diffuse-interface method to fully resolve the diffusion terms, which was also pointed out by Ruiz et al. (2016). Instead, the numerical or artificial dissipation, inherent in the numerical scheme or introduced by the subgrid-scale model, becomes the dominating diffusion effect when LES calculations are considered.

3.3. Analysis of numerical mixing processes

Due to the fact that molecular diffusion in the governing equations may not be fully resolved given the typical grid resolution in practical applications, we consider a binary mixture that is described by the one-dimensional Euler system of Eq. (1)

$$\frac{\partial}{\partial t} \begin{pmatrix} \rho \\ \rho u \\ \rho E \\ \rho Y \end{pmatrix} + \frac{\partial}{\partial x} \begin{pmatrix} \rho u \\ \rho u^2 + p \\ \rho u H \\ \rho u Y \end{pmatrix} = 0, \quad (24)$$

where $H = h + u^2/2$ is the specific total enthalpy. Here, we consider an advection problem of a density and mass fraction jump with initially constant pressure and velocity. A first-order upwinding scheme is considered for the spatial discretization with first-order explicit time integration. As discussed in the previous subsection, the thermodynamic pressure of the system is assumed to be constant. We also assume that pressure oscillations generated by the FC scheme are small. With this, we write $p = p_0 + p'$, where p_0 is the thermodynamic pressure and p' denotes the potentially spurious pressure oscillations.

For QC schemes, the pressure equilibrium will be maintained and the pressure and velocity will remain at the same constant value (Terashima and Koshi, 2012; Ma et al., 2017), so that $p' = 0$ and $u_{j-1}^n = u_j^n$, thus

$$\rho_j^{n+1} = \frac{\Delta t}{\Delta x} u_j^n \rho_{j-1}^n + \left(1 - \frac{\Delta t}{\Delta x} u_j^n\right) \rho_j^n, \quad (25a)$$

$$(\rho Y)_j^{n+1} = \frac{\Delta t}{\Delta x} u_j^n (\rho Y)_{j-1}^n + \left(1 - \frac{\Delta t}{\Delta x} u_j^n\right) (\rho Y)_j^n \quad (25b)$$

after one step of time advancement, where Δt is the time step and Δx is the grid spacing. By introducing $\xi = u_j^n \Delta t / \Delta x$, Eq. (25) can be rewritten as

$$\rho_j^{n+1} = \xi \rho_{j-1}^n + (1 - \xi) \rho_j^n, \quad (26a)$$

$$(\rho Y)_j^{n+1} = \xi (\rho Y)_{j-1}^n + (1 - \xi) (\rho Y)_j^n, \quad (26b)$$

which shows that the updated density and species are the result of the mixing of the two states from the previous time step. By using Eq. (26b), the mixing parameter ξ can be expressed as

$$\xi = \frac{(\rho Y)_j^{n+1} - (\rho Y)_j^n}{(\rho Y)_{j-1}^n - (\rho Y)_j^n}. \quad (27)$$

Upon inserting this expression into Eq. (26a) and after some rearrangement, we have

$$v_j^{n+1} = \frac{Y_j^{n+1} - Y_j^n}{Y_{j-1}^n - Y_j^n} v_{j-1}^n + \frac{Y_{j-1}^n - Y_j^{n+1}}{Y_{j-1}^n - Y_j^n} v_j^n, \quad (28)$$

which states that the updated specific volume and mass fraction are linearly related. This is equivalent to the definition of the isochoric mixing of Eq. (22).

For FC schemes, the pressure equilibrium across the contact interface will not be maintained, so that $p' \neq 0$. As a consequence, the velocity will not remain constant. However, due to the assumption that p' is small compared with the thermodynamic pressure p_0 , a constant thermodynamic pressure can be considered, and the energy equation in Eq. (24) is equivalent to the enthalpy equation,

$$\partial_t(\rho h) + \partial_x(\rho u h) = 0. \quad (29)$$

The discretized equations for mass, energy, and species are then written as

$$\rho_j^{n+1} = \frac{\Delta t}{\Delta x} u_{j-1}^n \rho_{j-1}^n + \left(1 - \frac{\Delta t}{\Delta x} u_{j-1}^n\right) \rho_j^n, \quad (30a)$$

$$(\rho h)_j^{n+1} = \frac{\Delta t}{\Delta x} u_{j-1}^n (\rho h)_{j-1}^n + \left(1 - \frac{\Delta t}{\Delta x} u_{j-1}^n\right) (\rho h)_j^n, \quad (30b)$$

$$(\rho Y)_j^{n+1} = \frac{\Delta t}{\Delta x} u_{j-1}^n (\rho Y)_{j-1}^n + \left(1 - \frac{\Delta t}{\Delta x} u_{j-1}^n\right) (\rho Y)_j^n, \quad (30c)$$

and the specific enthalpy and mass fraction at time t^{n+1} can be written as

$$h_j^{n+1} = \frac{\Delta t}{\Delta x} \frac{\rho_{j-1}^n}{\rho_j^{n+1}} u_{j-1}^n h_{j-1}^n + \left(1 - \frac{\Delta t}{\Delta x} u_{j-1}^n\right) \frac{\rho_j^n}{\rho_j^{n+1}} h_j^n, \quad (31a)$$

$$Y_j^{n+1} = \frac{\Delta t}{\Delta x} \frac{\rho_{j-1}^n}{\rho_j^{n+1}} u_{j-1}^n Y_{j-1}^n + \left(1 - \frac{\Delta t}{\Delta x} u_{j-1}^n\right) \frac{\rho_j^n}{\rho_j^{n+1}} Y_j^n. \quad (31b)$$

By defining

$$\zeta = \frac{\Delta t}{\Delta x} \frac{\rho_{j-1}^n}{\rho_j^{n+1}} u_{j-1}^n, \quad (32)$$

and using Eq. (30a), it follows

$$h_j^{n+1} = \zeta h_{j-1}^n + (1 - \zeta) h_j^n, \quad (33a)$$

$$Y_j^{n+1} = \zeta Y_{j-1}^n + (1 - \zeta) Y_j^n, \quad (33b)$$

which shows that for FC schemes, the specific enthalpy and mass fraction are determined from the mixing of the two states in the previous time step. The mixing parameter ζ can be expressed by the mass fraction as

$$\zeta = \frac{Y_j^{n+1} - Y_j^n}{Y_{j-1}^n - Y_j^n}, \quad (34)$$

and by combining this expression with Eq. (33a), we have

$$h_j^{n+1} = \frac{Y_j^{n+1} - Y_j^n}{Y_{j-1}^n - Y_j^n} h_{j-1}^n + \frac{Y_{j-1}^n - Y_j^{n+1}}{Y_{j-1}^n - Y_j^n} h_j^n, \quad (35)$$

which gives a linear relationship between the updated specific enthalpy and mass fraction. This is equivalent to the adiabatic mixing process described by Eq. (19).

With Eqs. (35) and (28), we have shown that for insufficient grid resolution the FC and QC schemes will follow the adiabatic and isochoric mixing models, respectively. These mixing behaviors are direct consequences of numerical diffusion inherent in the discretization schemes instead of the physical diffusion described by the diffusion laws in the governing equations.

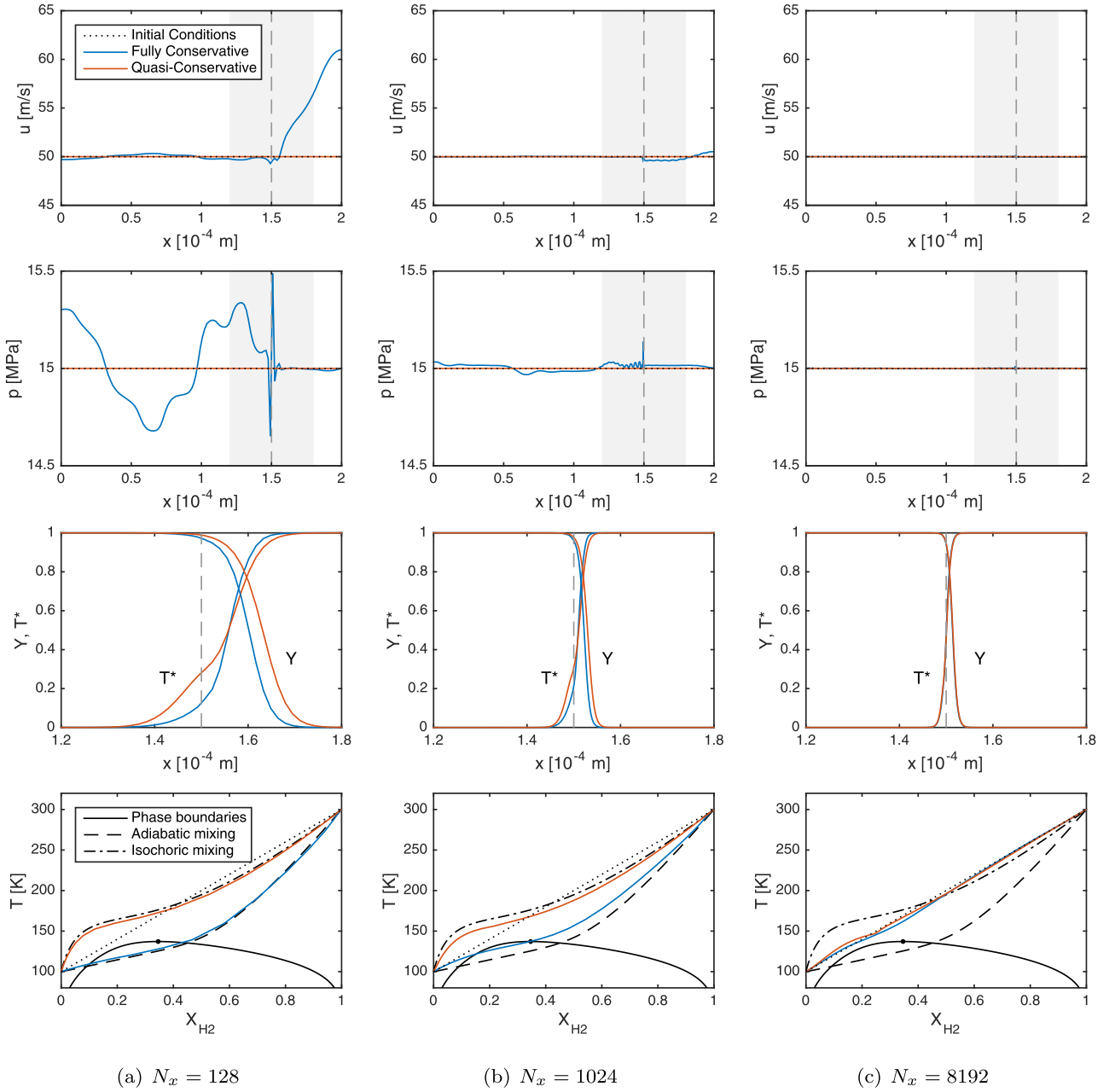


Fig. 6. Simulation results for one-dimensional advection of LOX/GH₂ interface at $t = 2 \mu\text{s}$ for three different mesh resolutions with both fully-conservative and quasi-conservative schemes. Velocity, pressure, normalized temperature and O₂ mass fraction profiles, and temperature-mole fraction diagram (from top to bottom). Pressure is at 15 MPa, O₂ is at 100 K, H₂ is at 300 K, and advection velocity is 50 m/s. Vertical dashed line denotes the location of the interface.

3.4. Numerical examples

To further illustrate the numerical mixing processes, we consider the one-dimensional advection of a LOX/GH₂ interface for different mesh resolutions. Note that the molecular diffusion terms are not considered, and the Euler system, Eq. (24), is solved. The computational domain has a length of 0.2 mm. Smooth interface profiles of temperature and O₂ mole fraction are placed at $x = 0.05 \text{ mm}$ initially, having the following form

$$T = \frac{T_{\text{H}_2} + T_{\text{O}_2}}{2} + \frac{T_{\text{H}_2} - T_{\text{O}_2}}{2} \tanh\left(\frac{x - x_0}{\epsilon}\right), \quad (36a)$$

$$X_{\text{O}_2} = \frac{1}{2} - \frac{1}{2} \tanh\left(\frac{x - x_0}{\epsilon}\right), \quad (36b)$$

where $x_0 = 0.05 \text{ mm}$ and $\epsilon = 0.001 \text{ mm}$ is the initial interface thickness. Oxygen is injected at the left boundary at 100 K, and the hydrogen has a temperature of 300 K. The pressure is set to 15 MPa. This gives a linear initial T - X mixing line as shown in the bottom of Fig. 6, and the initial mixing line lies outside the two-phase region compared to the phase boundaries. The velocity is set to 50 m/s initially, which is the same as the inlet velocity of the LOX stream. The pressure outlet is placed at the right boundary. A second-order ENO scheme (Ma et al., 2017) is used over the whole domain and the CFL number is set to 0.8. The simulation is run for $2 \mu\text{s}$ by which the interface advects 0.1 mm downstream.

It is worth noting that due to the energy conservation errors, QC schemes have limitations in correctly predicting the shock

speed when flows with strong shocks are considered (Abgrall and Karni, 2001), and several works were conducted to address this issue with QC schemes (Karni, 1996; Lee et al., 2013; Abgrall et al., 2018). However, applications for which the diffuse-interface methods, listed in Table 1, are developed for are typically low-speed flows in rocket combustion chambers, diesel engines, and gas turbines where shocks are rarely present. Therefore, the behavior of the numerical schemes in representing contact interface problems are the primary focus of this study.

Fig. 6 shows results using the FC and QC schemes for three different grid resolutions, namely $N_x = 128, 1024, \text{ and } 8192$. Velocity and pressure profiles at the end of the simulations are shown for the whole domain, and normalized temperature and O_2 mass fraction are shown in the region around the interface. The temperature is normalized as $T^* = (T - T_{O_2}) / (T_{H_2} - T_{O_2})$. For reference, the T - X mixing lines are shown together with adiabatic and isochoric mixing models as well as phase boundaries. As can be seen from Fig. 6(a), at relatively coarse resolution, pressure oscillations are generated by the FC scheme which introduces appreciable velocity perturbations superimposed to the advection speed. The QC scheme, on the other hand, maintains the pressure and velocity at the levels of the initial conditions. These results are consistent with the multi-dimensional test cases in previous studies (Terashima and Koshi, 2012; Ma et al., 2017). The pressure oscillations due to the FC scheme are alleviated with increasing resolution, and at a resolution of 8192 grid points, the solutions from FC and QC schemes for velocity and pressure collapse. This is due to the fact that the spurious pressure oscillations in the FC scheme and the energy conservation errors in the QC scheme both decrease with increasing resolution and indeed, the two schemes become identical in the continuous asymptotic limit.

Regarding the mixing behaviors, the temperature and mass fraction profiles predicted by the two schemes with low resolution are significantly different as can be seen in Fig. 6(a). The temperature calculated from the QC scheme is substantially higher than that from the FC scheme for the low temperature region on the LOX side, and a thicker mixing layer is predicted by the QC scheme. With increasing grid resolution, the profiles from the two schemes converge for both temperature and mass fraction, as shown in Fig. 6(c). For the mixing lines, at relatively low resolution, significant levels of numerical diffusion are introduced so that the adiabatic and isochoric mixing behaviors can be observed in Fig. 6(a). With increasing resolution, the mixing behaviors obtained from the different schemes start to deviate from these two limiting mixing conditions and eventually converge to the initial mixing line. Note that for this specific case, the initial conditions lie outside the two-phase region, however, for the underresolved FC scheme, a crossing of the mixing line with the phase boundary is obtained.

For the FC schemes, the numerical diffusion acts on the enthalpy and mass fraction in the same way as shown in Eq. (33) so that they are dissipated at the same rate. Therefore, a mixing behavior corresponding to unity Lewis number is expected. Indeed, additional numerical tests showed that with molecular diffusion considered, a fully resolved FC calculation with unity Lewis number assumption yields the adiabatic mixing line. In contrast, the QC scheme or the isochoric mixing model exhibits a behavior corresponding to faster heat transfer on the liquid side, which corresponds to a Lewis number greater than unity. We note that using fully resolved simulations with sophisticated diffusion models, previous studies have shown that a Lewis number significantly deviating from unity can be achieved under transcritical conditions (Yang et al., 1994; Harstad and Bellan, 1998; 1999), although a consensus regarding the diffusion processes for transcritical flows has yet to be reached. By comparing with available experimental measurements later in Section 4.3, it is quite clear that the adiabatic mixing model is inadequate in describing the mixing behav-

iors under transcritical conditions. As such, the use of the adiabatic mixing model for describing transcritical flows is called into question and the validity of this assumption requires further investigation.

4. Results and discussion

We proceed by considering two numerical test cases that are relevant for practical applications at transcritical conditions in Sections 4.1 and 4.2. Simulation results obtained from FC and QC schemes will be used for the analysis of different mixing behaviors. In Section 4.3, available measurements are utilized to relate these limiting mixing behaviors to experimental observations.

4.1. *n*-dodecane injection into N_2 environment

The first test case considers the injection of *n*-dodecane into a quiescent N_2 environment in two dimensions. The operating conditions correspond to the ECN Spray A case (Pickett and Bruneaux, 2011). The injection temperature of the *n*-dodecane jet is 363 K and the ambient environment is at a temperature of 900 K and a pressure of 6 MPa. The injection velocity is set to 100 m/s.

The computational domain has a dimension of $30h \times 16h$, where $h = 1.0$ mm is the height of the jet. A uniform mesh in both directions is employed, which has a minimum spacing of $0.02h$ with 50 grid points across the jet. The inlet condition of the jet is a plug flow with a top-hat velocity profile. Periodic boundary conditions are applied at top and bottom boundaries, and an adiabatic no-slip wall condition is prescribed at the left boundary. The pressure is specified at the outlet. The CFL number is set to a value of 0.8 and no sub-grid scale model is applied. Two simulations utilizing the FC scheme and the QC scheme with double-flux model are conducted.

Fig. 7 shows instantaneous fields of density and pressure at $t = 3.6$ ms towards the end of the simulations. For the FC scheme, the modification on the PR-EoS discussed in Section 2.2 is essential. Without this modification, we were not able to conduct the simulation due to the appearance of negative pressures. For the QC scheme, the modification is optional. As can be seen from Fig. 7, the two schemes predict similar density fields although results from the FC scheme show slightly more instabilities. However, significant pressure oscillations are generated by the FC scheme. In contrast, the QC scheme gives smooth pressure fields in which fluctuations are induced hydrodynamically. The results using the FC scheme are consistent with previous studies on transcritical flows (Terashima and Koshi, 2012; Ma et al., 2017). The grid resolution used in this case is finer than typical three-dimensional LES, and the magnitude of pressure oscillations are expected to increase with coarser meshes. Note that the results in Fig. 7(a) show that despite the fact that the EoS is modified to avoid the generation of negative pressures, spurious oscillations are still present.

Fig. 8 shows the instantaneous field of *n*-dodecane mass fraction and temperature at the same instant. The results for mass fraction are similar to those of density in Fig. 7, and both schemes predict similar behavior. However, significant differences can be observed in the temperature field. By comparing temperature fields obtained from different algorithms (Fig. 8(c) and (d)), it can clearly be seen that the temperature field calculated by the FC scheme is significantly lower than that computed using the double-flux model. These results are consistent with those reported by Matheis and Hickel (2016), and indicate the impact of the numerical scheme on the mixing behavior.

To quantify the numerical mixing behavior, we consider the composition space. The instantaneous simulation results from both schemes are plotted as scatter data in the form of T - X diagrams in Fig. 9, where X is the mole fraction of the more volatile

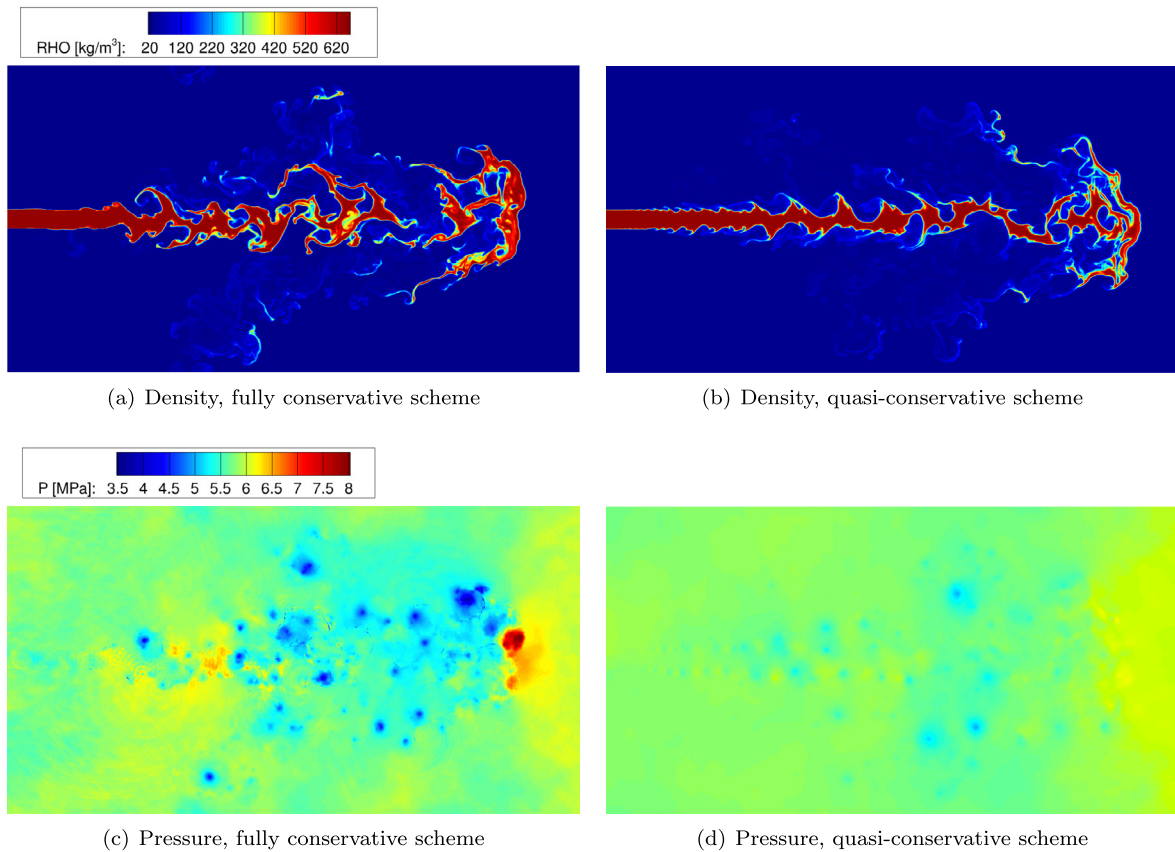


Fig. 7. Instantaneous fields of density (top) and pressure (bottom) for fully conservative (left) and quasi-conservative (right) schemes at $t = 3.6$ ms towards the end of the simulation for the n-dodecane injection case. The entire computational domain is shown.

component. The dew and bubble lines obtained from VLE calculations at three different pressure levels are also plotted to guide the analysis of phase separation. The pressure depicted by the solid black line is the nominal chamber pressure. Regions enclosed by the phase boundaries are two-phase regions. The mixing lines corresponding to the two mixing models, discussed in Section 3, are calculated with the PR-EoS, in which the constant environmental pressure is specified using the nominal chamber pressure.

It can be seen from Fig. 9 that the different numerical schemes yield two distinctly different T - X mixing lines, closely following the adiabatic and isochoric mixing models, as predicted from theoretical analysis. For the QC scheme, the fuel temperature rises first, followed by an approximately isothermal mixing process. In contrast, for the FC scheme, an almost isothermal mixing process starts first at the fuel side, followed by a rapid increase in temperature on the ambient N_2 side. LES calculations performed by Matheis and Hickel (2016) using both the FC scheme and the QC scheme with pressure evaluated from a transport equation are included in Fig. 9. The simulation results by Lacaze et al. (2015) using a FC scheme are plotted for comparison. It is interesting to see that results from both QC schemes collapse, and the three FC schemes follow very similar behavior. These results obtained from different numerical solvers are consistent with the analysis conducted in Section 3. For phase separation, due to the initial isothermal behavior in the FC schemes, a two-phase region is expected. However, for the results from the QC scheme, most of the solutions fall outside the phase boundaries and a two-phase flow is not expected. These results confirm the numerical analysis, showing that significantly different phase separation behaviors can be obtained from different numerical schemes.

4.2. LOX/GH2 mixing layer

The second case considered is more relevant for rocket engines, where a two-dimensional mixing layer of liquid oxygen (LOX) and gaseous hydrogen (GH2) is simulated. This case was proposed by Ruiz et al. (2016) as a benchmark case to test numerical solvers for high-Reynolds number flows with large density ratios. The LOX stream is injected at a temperature of 100 K, and GH2 is injected at a temperature of 150 K. The pressure is set to 10 MPa. The GH2 and LOX streams are injected at 125 m/s, and 30 m/s, respectively. For more details about the operating conditions of the benchmark case, the reader is referred to Ruiz et al. (2016).

The two streams are separated by the injector lip, which is also included in the computational domain. A domain of $15h \times 10h$ in axial and transversal directions is used, where $h = 0.5$ mm is the height of the injector lip. The region of interest extends from 0 to $10h$ in the axial direction with the origin set at the center of the lip face. A sponge layer of length $5h$ at the end of the domain is included to absorb acoustic waves. The computational mesh has 100 grid points across the injector lip, which is fine enough to give statistically converged solutions (Ruiz et al., 2016). A uniform mesh is used in both directions for the region from 0 to $10h$ in the axial direction and from $-1.5h$ to $1.5h$ in the transverse direction; stretching is applied with a ratio of 1.02 only in the transverse direction outside this region. Adiabatic no-slip wall conditions are applied at the injector lip and adiabatic slip wall conditions are applied at the top and bottom boundaries of the domain. A $1/7$ th power law for velocity is used for both the LOX and GH2 streams. The CFL number is set to 0.8 and no subgrid scale model is used. Simulations are conducted with both FC and QC schemes.

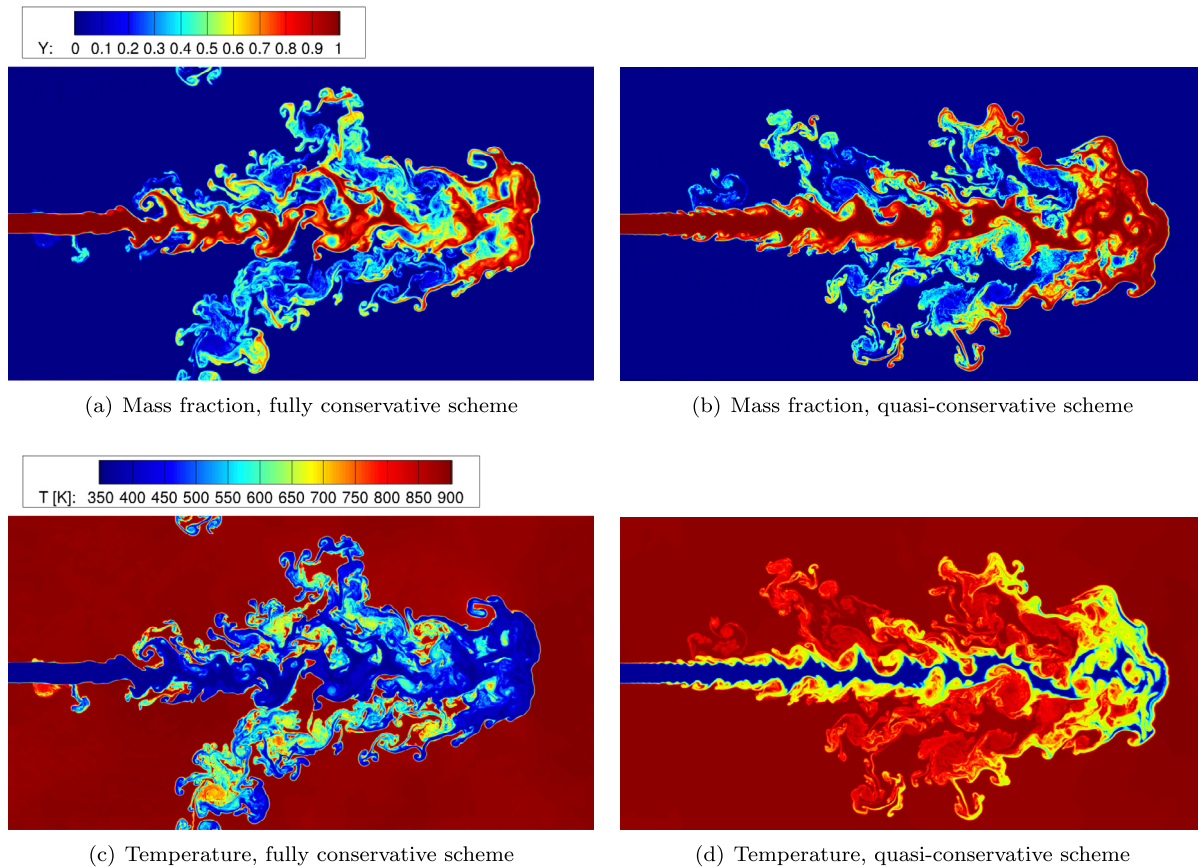


Fig. 8. Instantaneous fields of n-dodecane mass fraction (top) and temperature (bottom) for fully conservative (left) and quasi-conservative (right) schemes at $t = 3.6$ ms towards the end of the simulation for the n-dodecane injection case. The entire computational domain is shown.

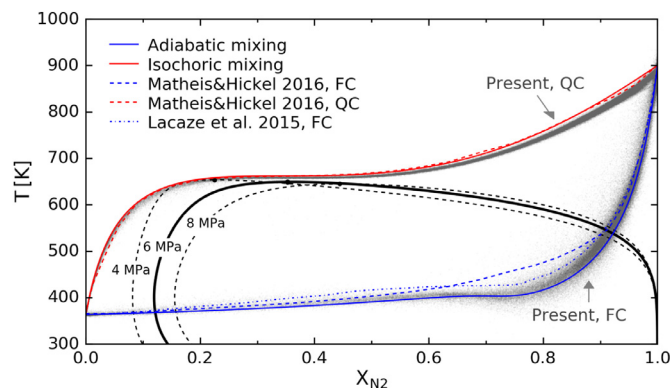


Fig. 9. T-X diagram for the n-dodecane injection case. Scatter data from simulation results in Section 4.1 for two different numerical schemes. FC is short for fully conservative and QC for quasi-conservative. Phase boundaries from VLE calculations are shown in black for three pressures. Simulation results from Lacaze et al. (2015) (FC scheme) and Matheis and Hickel (2016) (both FC and QC schemes) are also shown for reference.

Fig. 10 shows results for instantaneous fields of density, pressure, O_2 mass fraction and temperature computed by both schemes. For the density field, “comb-like” structures (Mayer et al., 2000; Ruiz, 2012) can be seen for both schemes. This was also observed experimentally under typical rocket engine conditions (Mayer et al., 2000; Oswald et al., 2006; Chehroudi, 2012). Spurious pressure oscillations can clearly be seen with the FC scheme. These pressure oscillations are mostly generated in the oxygen stream and result from insufficient resolution of thermodynamic non-linearities, which was also discussed in Section 3.4.

Despite the similar behavior in the mass fraction field, the temperature field shows a significantly different behavior. In particular, the temperature field predicted by the double-flux model is significantly higher than that predicted by the FC scheme. Similar behavior was also observed for the n-dodecane injection case.

The flow field was averaged over 15 flow-through-times after reaching steady state, with one flow-through-time corresponding to 0.125 ms (Ruiz et al., 2016). Mean and rms results for O_2 mass fraction and temperature are shown in Fig. 11. Statistics at different axial locations ($x/h = 1, 3, 5, 7$) are plotted as a function of normalized transverse distance. The results obtained in the benchmark case (Ruiz et al., 2016) are also included for comparison. These results were computed using the solvers AVBP and RAPTOR, as listed in Table 1. AVBP uses a QC scheme for the simulation of transcritical flows, whereas RAPTOR is a FC solver with a dual time-stepping scheme. Fig. 11 shows that a good agreement for the O_2 mass fraction between the FC and QC schemes with the solver CharLES^x, and the mean and rms values collapse for both schemes. Similar trends can be observed for the other two solvers. However, results obtained from CharLES^x show slight discrepancies from the other two solvers, which is reflected by a narrower shear layer on the hydrogen side. These discrepancies were attributed to the different implementations of the sponge layer and outlet boundary conditions adopted by the different solvers (Lacaze, 2016).

Considering the mean and rms results for the temperature field shown in Fig. 11, it can clearly be seen that two distinct behaviors are present; one obtained by the FC schemes and the other by the QC schemes. Similar to the trends seen in Fig. 10, the mean temperature obtained by the QC schemes is significantly higher than that obtained by the FC schemes and the thermal mix-

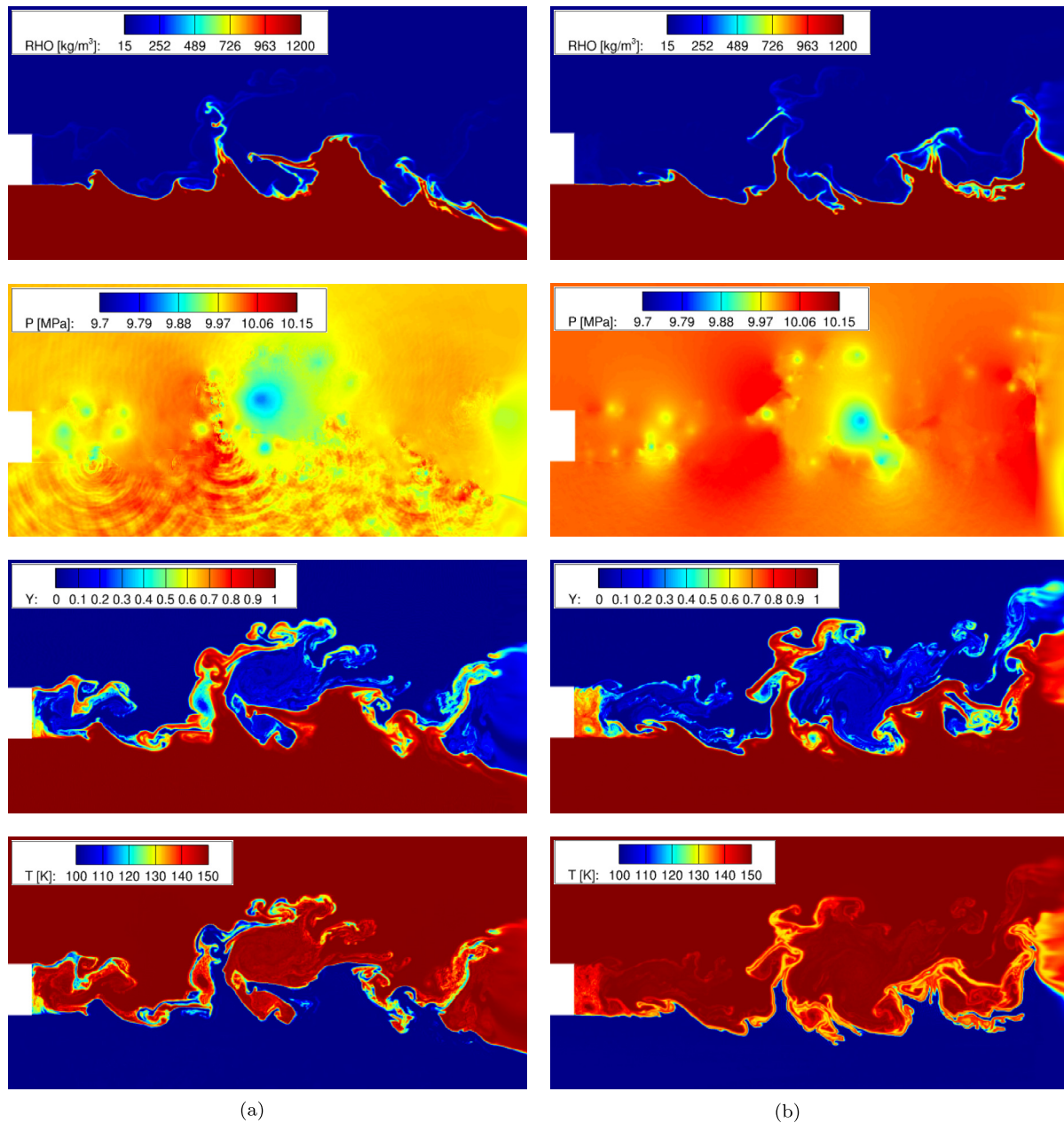


Fig. 10. Instantaneous fields of density, pressure, O_2 mass fraction, and temperature from top to bottom for (a) the fully conservative scheme and (b) the quasi-conservative scheme with double-flux model for the LOX/GH₂ mixing case.

ing layer is much narrower, which is more clearly seen by the rms results. Note that these results are obtained from three different numerical solvers, and although in this study the numerical discretization within CharLES^x is kept identical for FC and QC schemes, the numerics from the other two solvers differ significantly. Moreover, the QC schemes used by AVBP and CharLES^x are distinctly different. The surprisingly similar behavior in the temperature field observed here is merely determined by whether the numerical solver is fully conservative or not.

The instantaneous simulation results are plotted as scatter data in the form of T - X diagrams in Fig. 12 along with the simulation results from Lacaze and Oefelein (2013). The adiabatic and isochoric mixing lines are also shown for comparison. Results for the LOX/GH₂ mixing layer case follow similar trends as seen in Fig. 9. The FC schemes from Lacaze and Oefelein (2013) and the present work predict a substantially lower temperature with an

approximately isothermal mixing process on the LOX side compared to the sharp increase of temperature predicted by the QC scheme. The mixing behaviors follow closely the two limiting thermodynamic mixing models due to the prevailing numerical dissipation effects. In terms of phase behavior, both schemes predict states within the two-phase region, although the QC scheme has the smaller percentage of solutions falling in the region of phase separation.

These test cases show that distinctly different mixing behaviors corresponding to two asymptotic mixing models are observed for FC and QC schemes, even across different numerical solvers. Specifically, the temperature fields predicted by the QC schemes are significantly higher than those obtained from the FC schemes, resulting in significantly different predictions of phase separation. These differences in the mixing behaviors have a direct consequence on

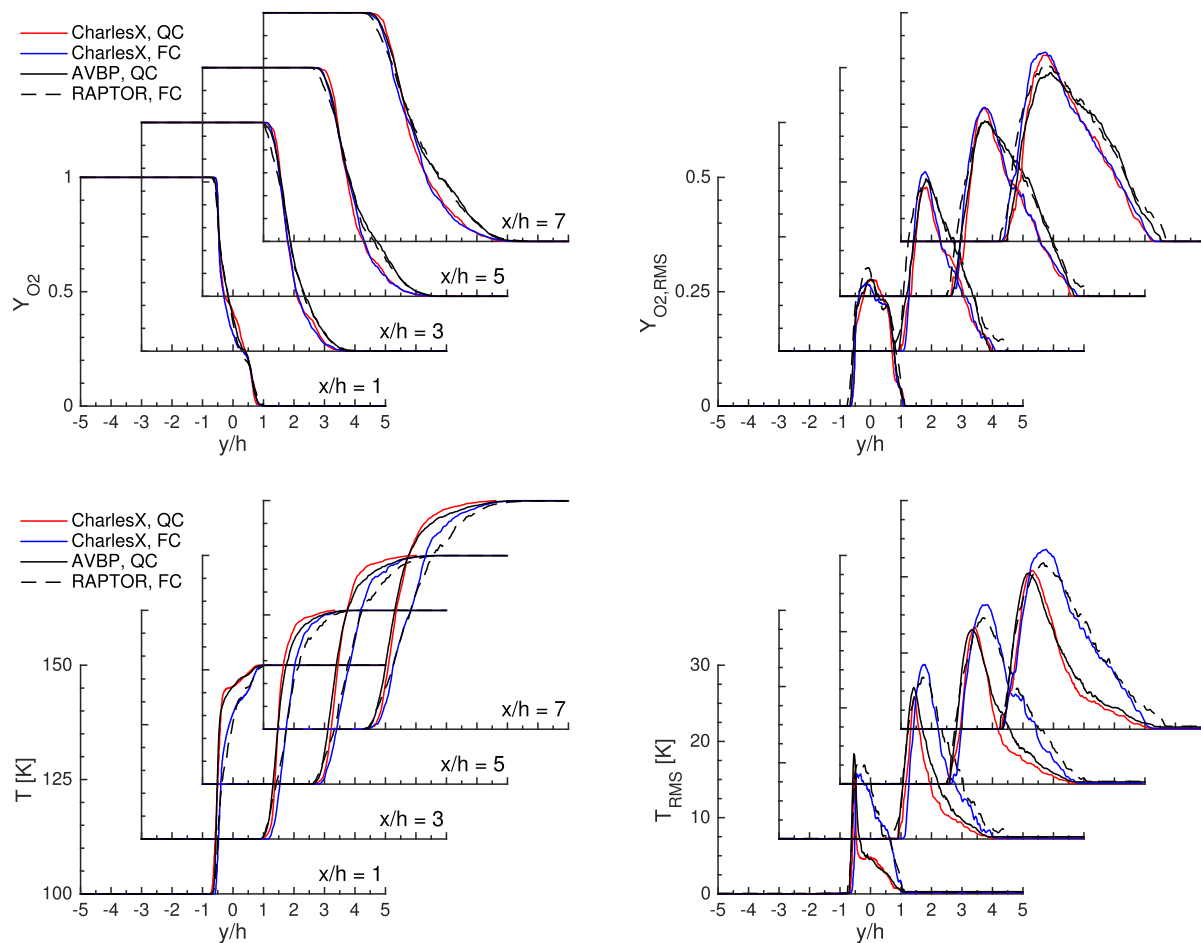


Fig. 11. Transverse cuts of mean (left) and rms (right) of oxygen mass fraction (top) and temperature (bottom) of the LOX/GH₂ mixing case. FC is short for fully conservative and QC for quasi-conservative.

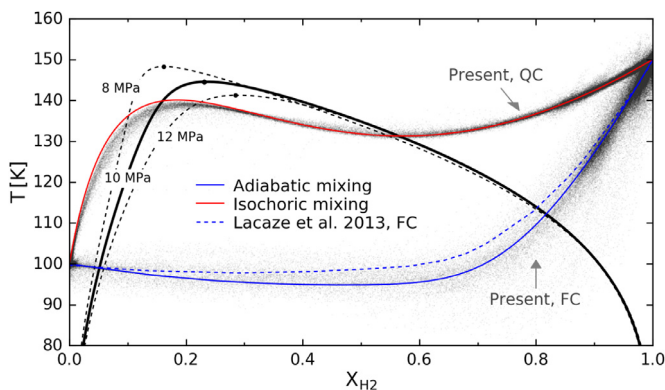


Fig. 12. T - X diagram for the LOX/GH₂ mixing layer case. Scatter data from simulation results in Section 4.2 for two different numerical schemes. Phase boundaries from VLE calculations are shown in black for three pressures. Simulation results from Lacaze and Oefelein (2013) (FC scheme) are also shown for reference.

the subsequent processes following the mixing, e.g. ignition and combustion.

4.3. Comparison with experiments

In Section 3 and previous subsections, we have identified that the mixing processes predicted by the FC and QC schemes can be represented by the limiting conditions of adiabatic and isochoric

mixing merely from thermodynamic analysis. Here, the two mixing models are employed to study the phase separation behaviors and compare with available experimental measurements.

4.3.1. *n*-dodecane injection

The first set of experiments considered is the *n*-dodecane injection conducted by Manin et al. (2014). In these experiments, the fuel is injected at a temperature of 363 K into a N₂ environment. The chamber pressure and temperature are varied to identify conditions where droplets and ligaments can be observed experimentally to confirm the phase separation. Here, the adiabatic and isochoric mixing lines are calculated at different chamber pressures and temperatures, along with the VLE phase boundaries calculated at the corresponding pressure. Results for several representative conditions are shown in Fig. 13. It can be seen that, since *n*-dodecane is injected at a relatively low temperature with a reduced temperature of $T_r = 0.55$, the initial isothermal behavior of the adiabatic mixing intersects the mixing line with the two-phase region regardless of ambient pressure and temperature. Even at a pressure of 12 MPa and an ambient temperature of 1500 K, a large portion of the solution falls inside the two-phase region. In contrast, the region occupied by the two-phase flow significantly reduces for the isochoric mixing as the chamber pressure and temperature increase.

The percentage of the solutions intersecting the two-phase region from the two mixing models is extracted from the calculations and shown in Fig. 14 as contour in the p - T state space. A

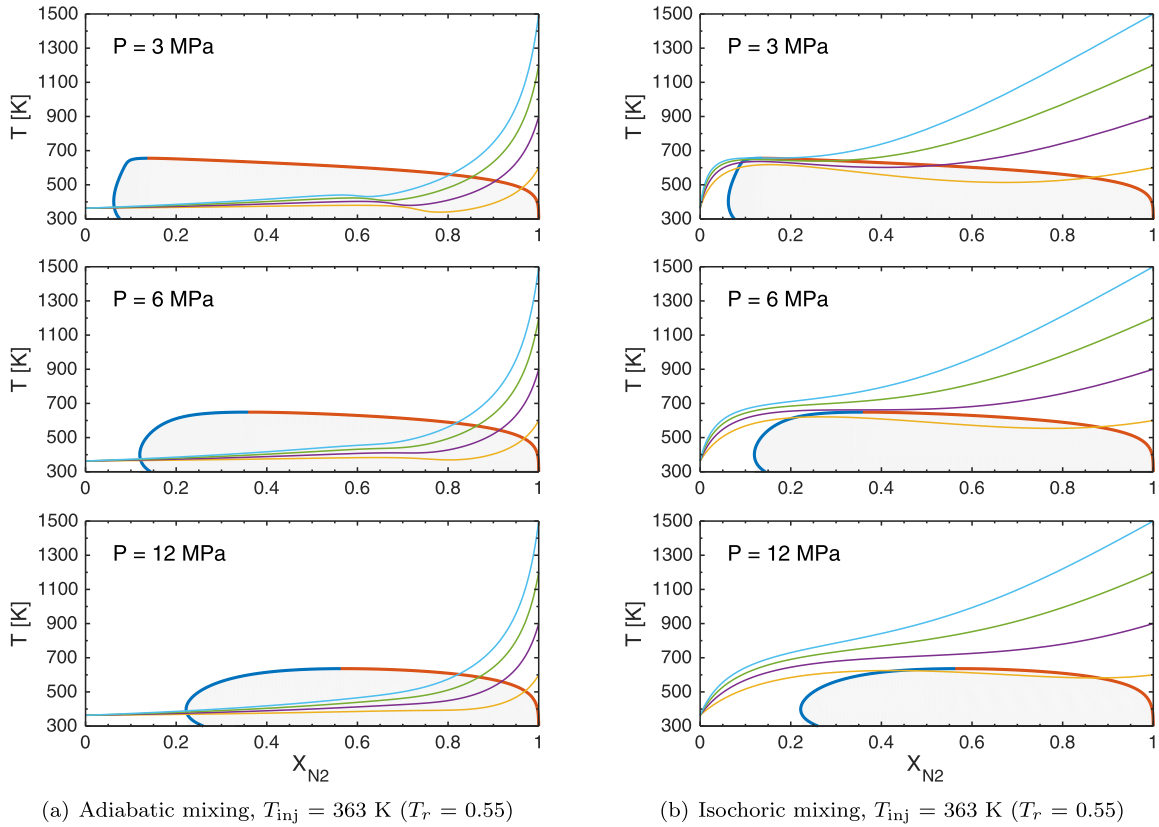


Fig. 13. T - X diagrams for n-dodecane injection into N_2 environment predicted by (a) adiabatic and (b) isochoric mixing models at different pressures. n-Dodecane is injected at 363 K ($T_r = 0.55$) and different ambient temperatures for N_2 are considered (600, 900, 1200, 1500 K). Phase boundaries from VLE calculations are also shown for reference.

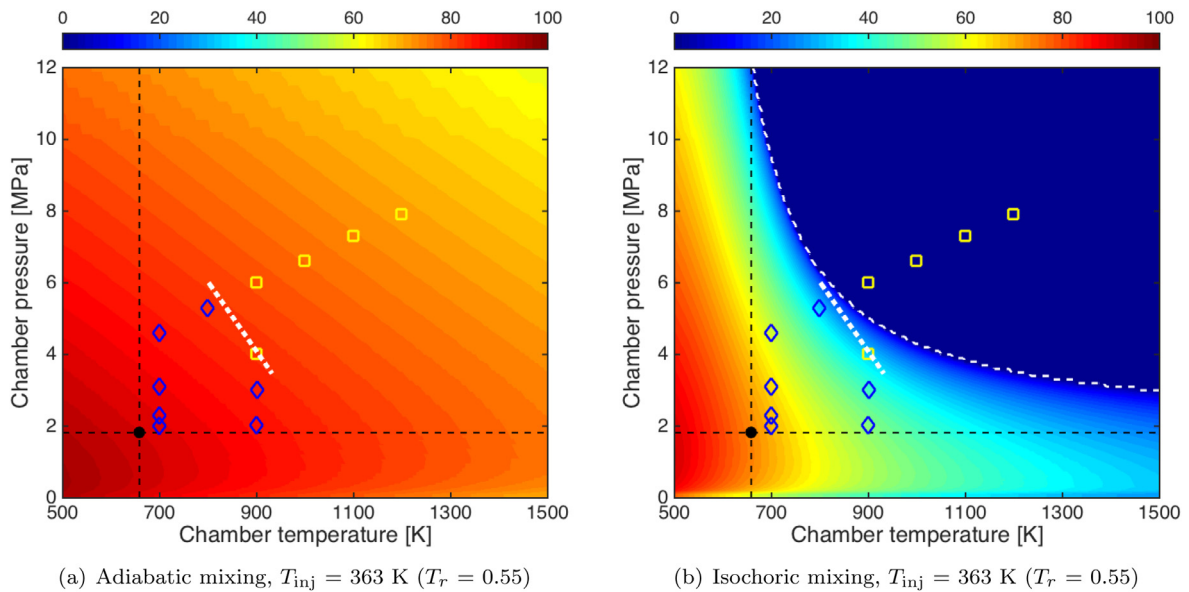


Fig. 14. p - T diagram of operating conditions (chamber pressure against ambient temperature) of n-dodecane injection into N_2 environment. Contours of percentage of two-phase region occupied by (a) adiabatic and (b) isochoric mixing models are shown in comparison with experimental measurements by Manin et al. (2014). The black dot is the critical point of n-dodecane. Blue diamonds are conditions representing classical spray breakup in experiments, and yellow squares correspond to conditions where ligaments or droplet breakup are not observed experimentally. The white dotted and dashed lines are the estimation of the transition given by Manin et al. (2014) and isochoric mixing, respectively. (For interpretation of the references to colour in this figure legend, the reader is referred to the web version of this article.)

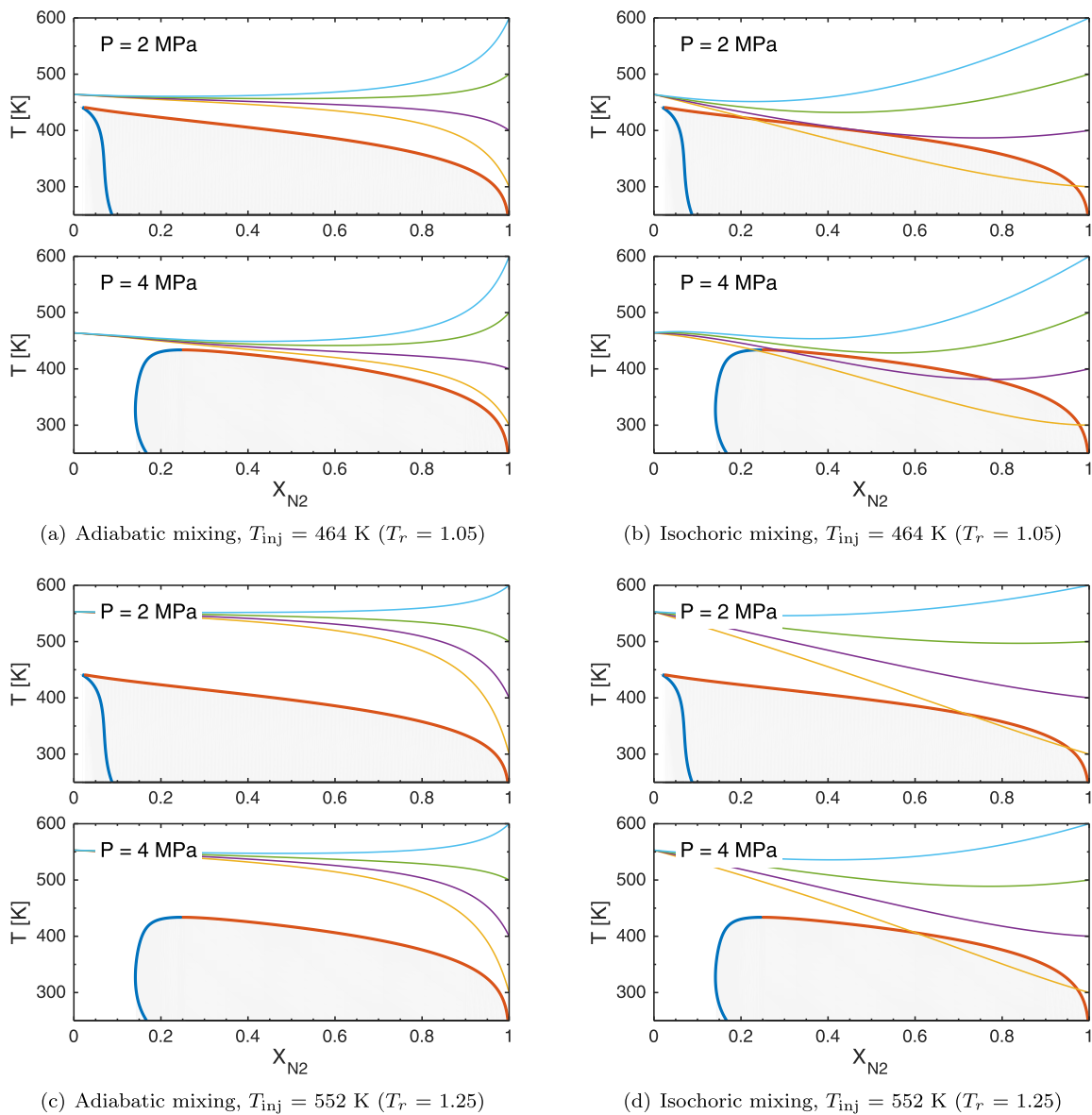


Fig. 15. T - X diagrams for fluoroketone injection into N_2 environment predicted by (a, c) adiabatic and (b, d) isochoric mixing models at different pressures for two injection temperatures of (a, b) 464 K ($T_r = 1.05$) and (c, d) 552 K ($T_r = 1.25$). Different ambient temperatures for N_2 are considered (300, 400, 500, 600 K). Phase boundaries from VLE calculations are also shown for reference.

value of zero in these plots indicates that all states fall outside the regions of phase separation. The experimental measurements by Manin et al. (2014) are also shown for comparison. As can be seen from Fig. 14(a), phase separation is predicted over the whole state space with a percentage always above fifty percent. For the case of isochoric mixing, as shown in Fig. 14(b), the percentage of states falling in the two-phase region reduces with increasing chamber temperature and pressure, and a clear boundary can be obtained. Based on the measurements, Manin et al. (2014) estimated a transition line that separates the subcritical and supercritical behaviors as observed in the experiments, which are shown as white dotted lines in Fig. 14. This transition behavior is completely missing based on the results from adiabatic mixing, whereas the results from isochoric mixing are in qualitative agreement with the experiments.

4.3.2. Fluoroketone injection

The second set of experiments considered was conducted by Roy et al. (2013), where fluoroketone is injected into a N_2 cham-

ber. In these experiments, the injection temperature is varied in addition to the chamber pressure and chamber temperature. In comparison with the experiments by Manin et al. (2014), the injection temperature is relatively high, with reduced temperature mostly greater than unity. Through analysis of their measurements, Roy et al. (2013) proposed a criterion to determine whether droplets and surface tension effects are present. Specifically, they observed that for conditions where

$$p_{r,ch} > 1, \quad T_{r,inj} \times T_{r,ch} > 0.975, \quad (37)$$

complete supercritical behavior is expected, where $T_{r,inj}$ is the reduced injection temperature and $p_{r,ch}$ and $T_{r,ch}$ are the reduced chamber pressure and temperature, respectively.

For the analysis considered here, two representative injection temperatures are considered and the chamber pressure and temperature are varied. Results of mixing lines for representative chamber conditions are shown in Fig. 15, along with the phase boundaries from VLE calculations. With higher injection temperatures, adiabatic mixing generates isothermal processes, initially

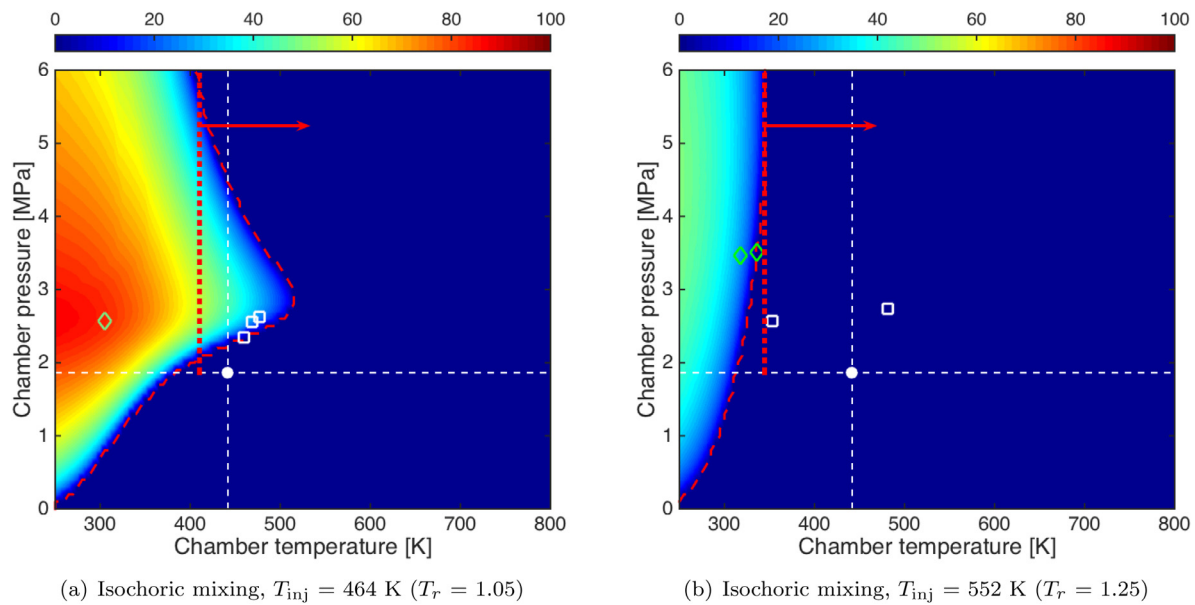


Fig. 16. p - T diagram of operating conditions (chamber pressure against ambient temperature) of fluoroketone injection into N_2 environment for two injection temperatures. Contours of percentage of two-phase region occupied by the isochoric mixing model are shown in comparison with experimental measurements by Roy et al. (2013). The adiabatic mixing model predicts no two-phase behavior over all operating conditions shown. The white dot is the critical point of fluoroketone. Green diamonds are conditions under which droplets are observed in experiments, and white squares correspond to conditions where droplets and surface tension effects are not observed experimentally. The red dotted and dashed lines are the transition given by the criterion proposed by Roy et al. (2013) (Eq. (37)) and isochoric mixing, respectively. (For interpretation of the references to colour in this figure legend, the reader is referred to the web version of this article.)

starting from the fuel side, and the temperature starts to increase or decrease close to the N_2 side depending on the ambient temperature. This behavior of the adiabatic mixing model at high injection temperature prevents the mixing lines from entering the two-phase region, even at very low ambient temperature. In contrast, the mixing lines calculated by the isochoric mixing model show approximately linear behavior between the fuel and ambient conditions, especially for the case with higher injection temperature, as seen from Fig. 15(d). When the ambient temperature is low, the mixing lines from isochoric mixing enter the two-phase region.

Similar to the analysis of the n-dodecane injection case, the percentage of the solutions intersecting the two-phase region is extracted from the calculations and shown in p - T state diagrams in Fig. 16. The experimental measurements with injection temperatures that are close to the two temperature values considered are also included. The criterion of Eq. (37) proposed by Roy et al. (2013) is shown as red dotted line and the regions where no droplets or ligaments are expected are depicted by red arrows. For the adiabatic mixing model, two-phase behavior is not obtained for all chamber conditions and the two injection temperatures considered. This is in conflict with the experimental measurements by Roy et al. (2013), where at lower chamber temperatures, droplets can clearly be seen downstream of the jet from the PLIF images. In contrast, the isochoric mixing is able to predict a clear transition boundary for both injection temperatures considered, and the predictions are in qualitative agreement with measurements. An interesting phenomena which can be seen from Fig. 16 is that it may be harder to enter the two-phase region under subcritical pressures for the cases considered here with high injection temperatures. This can be explained by the fact that when the pressure becomes subcritical with respect to the fuel, the critical point on the phase boundaries becomes the saturation pressure point on the pure fuel side, and this saturation pressure will decrease with ambient pressure, reducing the possibility of phase separation for lower chamber pressures.

In summary, the results for the cases considered for different fuels, injection temperatures, and chamber conditions, along with comparisons with experimental measurements indicate that it may be inadequate to utilize the commonly used adiabatic mixing model to delineate the phase separation of transcritical flows.

5. Conclusions

The impact of different numerical schemes of commonly used diffuse-interface methods on the mixing processes for transcritical flows is investigated. To this end, two classes of schemes are examined, namely the fully conservative (FC) and the quasi-conservative (QC) schemes. Through the analysis of multi-dimensional simulation results, theoretical derivations, and comparisons with available experimental measurements, the following conclusions are drawn:

- The cause for failures of previous simulations reported in the literature using FC schemes is attributed to the generation of negative pressures due to the behavior of the cubic equation of state (EoS) inside the vapor dome. With modifications to the EoS, simulations with the FC scheme can be stabilized. Spurious pressure oscillations, although more severe compared to simulations of ideal-gas flows, may not be the key reason for the failure of the simulations.
- Significant spurious pressure oscillations are observed in both multi-dimensional cases for the FC scheme, which is consistent with findings from previous studies (Terashima and Koshi, 2012; Kawai et al., 2015; Pantano et al., 2017; Ma et al., 2017).
- Numerical analysis shows that under conditions relevant to practical applications, the typical mesh resolution is inadequate to fully resolve the diffusion processes, and mixing is dominated by numerical dissipation.
- Through analysis of the numerical diffusion inherent in the up-winding schemes, it is shown that for underresolved solutions, FC and QC schemes behave as the limiting cases of isobaric-adiabatic and isobaric-isochoric mixing models for binary mixtures. These limiting mixing conditions are confirmed by nu-

merical simulation results, characterized by significantly different temperature fields predicted by the two schemes.

- Analysis of existing measurements at transcritical conditions suggests that the phase separation behavior predicted by the commonly used adiabatic mixing model is inconsistent with experiments.

This study provides insight into the interpretation of simulation results of transcritical flows, and explains that it may be inappropriate to utilize the adiabatic mixing model for the validation of simulation results. It is also questionable to use the adiabatic mixing line to study the phase separation behavior for transcritical flows. Further experimental and computational investigations are therefore needed to clarify the physical mixing and phase separation behaviors of transcritical flows.

Acknowledgments

Financial support through Army Research Laboratory with award number W911NF-16-2-0170 and National Aeronautics and Space Administration (NASA) with award number NNX15AV04A is gratefully acknowledged. Part of this work was inspired by the discussion with Dr. Jan Matheis and Prof. Stefan Hickel during the Summer Program 2016. Resources supporting this work were provided by the NASA High-End Computing (HEC) Program through the NASA Advanced Supercomputing (NAS) Division at Ames Research Center.

References

- Abgrall, R., 1996. How to prevent pressure oscillations in multicomponent flow calculations: a quasi conservative approach. *J. Comput. Phys.* 125 (1), 150–160.
- Abgrall, R., Bacigaluppi, P., Tokareva, S., 2018. A high-order nonconservative approach for hyperbolic equations in fluid dynamics. *Comput. Fluids* 169, 10–22.
- Abgrall, R., Karni, S., 2001. Computations of compressible multifluids. *J. Comput. Phys.* 169 (2), 594–623.
- Banuti, D.T., Ma, P.C., Hickey, J.-P., Ihme, M., 2018. Thermodynamic structure of supercritical LOX–GH₂ diffusion flames. *Combust. Flame* 196, 364–376.
- Banuti, D.T., Raju, M., Ma, P.C., Ihme, M., Hickey, J.-P., 2017. Seven questions about supercritical fluids—towards a new fluid state diagram. 55th AIAA Aerospace Sciences Meeting. Grapevine, TX.
- Bellan, J., 2000. Supercritical (and subcritical) fluid behavior and modeling: drops, streams, shear and mixing layers, jets and sprays. *Prog. Energy Combust. Sci.* 26 (4), 329–366.
- Billet, G., Abgrall, R., 2003. An adaptive shock-capturing algorithm for solving unsteady reactive flows. *Comput. Fluids* 32 (10), 1473–1495.
- Billet, G., Ryan, J., 2011. A Runge–Kutta discontinuous Galerkin approach to solve reactive flows: the hyperbolic operator. *J. Comput. Phys.* 230 (4), 1064–1083.
- Candel, S., Juniper, M., Singla, G., Scoufflaire, P., Rolon, C., 2006. Structures and dynamics of cryogenic flames at supercritical pressure. *Combust. Sci. Technol.* 178, 161–192.
- Chehroudi, B., 2012. Recent experimental efforts on high-pressure supercritical injection for liquid rockets and their implications. *Int. J. Aerosp. Eng.* 2012, 1–31.
- Chung, T.H., Lee, L.L., Starling, K.E., 1984. Applications of kinetic gas theories and multiparameter correlation for prediction of dilute gas viscosity and thermal conductivity. *Ind. Eng. Chem. Res.* 23 (1), 8–13.
- Dahms, R.N., Manin, J., Pickett, L.M., Oefelein, J.C., 2013. Understanding high-pressure gas–liquid interface phenomena in Diesel engines. *Proc. Combust. Inst.* 34 (1), 1667–1675.
- Dahms, R.N., Oefelein, J.C., 2015. Non-equilibrium gas–liquid interface dynamics in high-pressure liquid injection systems. *Proc. Combust. Inst.* 35 (2), 1587–1594.
- Delplanque, J.-P., Sirignano, W., 1993. Numerical study of the transient vaporization of an oxygen droplet at sub- and super-critical conditions. *Int. J. Heat Mass Transfer* 36 (2), 303–314.
- Elliott, J., Lira, C., 2012. *Introductory Chemical Engineering Thermodynamics*. Prentice Hall.
- Ely, J.F., Hanley, H., 1981. Prediction of transport properties. 1. Viscosity of fluids and mixtures. *Ind. Eng. Chem. Res.* 20 (4), 323–332.
- Ely, J.F., Hanley, H., 1983. Prediction of transport properties. 2. Thermal conductivity of pure fluids and mixtures. *Ind. Eng. Chem. Res.* 22 (1), 90–97.
- Gomez, H., Hughes, T.J.R., Nogueira, X., Calo, V.M., 2010. Isogeometric analysis of the isothermal Navier–Stokes–Korteweg equations. *Comput. Methods Appl. Mech. Eng.* 199 (25), 1828–1840.
- Gottlieb, S., Shu, C.-W., Tadmor, E., 2001. Strong stability-preserving high-order time discretization methods. *SIAM Rev.* 43 (1), 89–112.
- Habiballah, M., Orain, M., Grisch, F., Vingert, L., Gicquel, P., 2006. Experimental studies of high-pressure cryogenic flames on the Mascotte facility. *Combust. Sci. Technol.* 178, 101–128.
- Haldenwang, P., Nicoli, C., Daou, J., 1996. High pressure vaporization of LOX droplet crossing the critical conditions. *Int. J. Heat Mass Transfer* 39 (16), 3453–3464.
- Ham, F., Iaccarino, G., 2004. *Energy Conservation in Collocated Discretization Schemes on Unstructured Meshes*. Annual Research Briefs. Center for Turbulence Research, Stanford University.
- Harstad, K., Bellan, J., 1998. Isolated fluid oxygen drop behavior in fluid hydrogen at rocket chamber pressures. *Int. J. Heat Mass Transfer* 41, 2426–2449.
- Harstad, K., Bellan, J., 1999. The Lewis number under supercritical conditions. *Int. J. Heat Mass Transfer* 42 (6), 961–970.
- Harstad, K., Bellan, J., 2000. An all-pressure fluid drop model applied to a binary mixture: heptane in nitrogen. *Int. J. Multiphase Flow* 26 (10), 1675–1706.
- Harstad, K.G., Miller, R.S., Bellan, J., 1997. Efficient high-pressure state equations. *AIChE J.* 43 (6), 1605–1610.
- Hickey, J.-P., Ma, P.C., Ihme, M., Thakur, S., 2013. Large eddy simulation of shear coaxial rocket injector: Real fluid effects. In: 49th AIAA/ASME/SAE/ASEE Joint Propulsion Conference. San Jose, CA.
- Karni, S., 1994. Multicomponent flow calculations by a consistent primitive algorithm. *J. Comput. Phys.* 112 (1), 31–43.
- Karni, S., 1996. Hybrid multifluid algorithms. *SIAM J. Sci. Comput.* 17 (5), 1019–1039.
- Kawai, S., Terashima, H., Negishi, H., 2015. A robust and accurate numerical method for transcritical turbulent flows at supercritical pressure with an arbitrary equation of state. *J. Comput. Phys.* 300, 116–135.
- Khalighi, Y., Nichols, J.W., Lele, S., Ham, F., Moin, P., 2011. Unstructured large eddy simulation for prediction of noise issued from turbulent jets in various configurations. In: 17th AIAA/CEAS Aeroacoustics Conference. Portland, OR.
- Knudsen, E., Doran, E.M., Mittal, V., Meng, J., Spurlock, W., 2017. Compressible Eulerian needle-to-target large eddy simulations of a diesel fuel injector. *Proc. Combust. Inst.* 36 (2), 2459–2466.
- Lacaze, G., 2016. Private communication.
- Lacaze, G., Misdaris, A., Ruiz, A., Oefelein, J.C., 2015. Analysis of high-pressure Diesel fuel injection processes using LES with real-fluid thermodynamics and transport. *Proc. Combust. Inst.* 35 (2), 1603–1611.
- Lacaze, G., Oefelein, J.C., 2012. A non-premixed combustion model based on flame structure analysis at supercritical pressures. *Combust. Flame* 159 (6), 2087–2103.
- Lacaze, G., Oefelein, J.C., 2013. Modeling of high density gradient flows at supercritical pressures. In: 49th AIAA/ASME/SAE/ASEE Joint Propulsion Conference. San Jose, CA.
- Lacaze, G., Ruiz, A., Schmitt, T., Oefelein, J.C., 2017. Robust treatment of thermodynamic nonlinearities in the simulation of transcritical flows. In: SIAM 16th International Conference on Numerical Combustion. Orlando, FL.
- Lee, B.J., Toro, E.F., Castro, C.E., Nikiforakis, N., 2013. Adaptive Osher-type scheme for the Euler equations with highly nonlinear equations of state. *J. Comput. Phys.* 246, 165–183.
- Lv, Y., Ihme, M., 2014. Discontinuous Galerkin method for multi-component chemically reacting flows and combustion. *J. Comput. Phys.* 270, 105–137.
- Ma, P.C., Bravo, L., Ihme, M., 2014. Supercritical and transcritical real-fluid mixing in diesel engine applications. In: Proceedings of the Summer Program, Center for Turbulence Research, Stanford University, pp. 99–108.
- Ma, P.C., Lv, Y., Ihme, M., 2017. An entropy-stable hybrid scheme for simulations of transcritical real-fluid flows. *J. Comput. Phys.* 340, 330–357.
- Manin, J., Bardi, M., Pickett, L.M., Dahms, R.N., Oefelein, J.C., 2014. Microscopic investigation of the atomization and mixing processes of diesel sprays injected into high pressure and temperature environments. *Fuel* 134, 531–543.
- Matheis, J., Hickel, S., 2016. Multi-component vapor–liquid equilibrium model for LES and application to ECN Spray A. In: Proceedings of the Summer Program. Center for Turbulence Research, Stanford University, pp. 25–34.
- Matheis, J., Hickel, S., 2018. Multi-component vapor–liquid equilibrium model for LES of high-pressure fuel injection and application to ECN Spray A. *Int. J. Multiphase Flow* 99, 294–311.
- Mayer, W., Schik, A., Schaffler, M., Tamura, H., 2000. Injection and mixing processes in high-pressure liquid oxygen/gaseous hydrogen rocket combustors. *J. Propul. Power* 16 (5), 823–828.
- Mayer, W., Schik, A., Vielle, V., Chauveau, C., Gökalp, I., Talley, D.G., Woodward, R.D., 1998. Atomization and breakup of cryogenic propellants under high-pressure subcritical and supercritical conditions. *J. Propul. Power* 14, 835–842.
- Mayer, W., Tamura, H., 1996. Propellant injection in a liquid oxygen/gaseous hydrogen rocket engine. *J. Propul. Power* 12 (6), 1137–1147.
- Meng, H., Yang, V., 2003. A unified treatment of general fluid thermodynamics and its application to a preconditioning scheme. *J. Comput. Phys.* 189 (1), 277–304.
- Menikoff, R., Plohr, B.J., 1989. The Riemann problem for fluid flow of real materials. *Rev. Mod. Phys.* 61 (1), 75.
- Miller, R.S., Bellan, J., 1999. Direct numerical simulation of a confined three-dimensional gas mixing layer with one evaporating hydrocarbon-droplet-laden stream. *J. Fluid Mech.* 384, 293–338.
- Miller, R.S., Harstad, K.G., Bellan, J., 2001. Direct numerical simulations of supercritical fluid mixing layers applied to heptane–nitrogen. *J. Fluid Mech.* 436, 1–39.
- Müller, H., Niedermeier, C.A., Matheis, J., Pfützner, M., Hickel, S., 2016. Large-eddy simulation of nitrogen injection at trans- and supercritical conditions. *Phys. Fluids* 28 (1), 015102.
- Newman, J., Brzustowski, T., 1971. Behavior of a liquid jet near the thermodynamic critical region. *AIAA J.* 9 (8), 1595–1602.
- Oefelein, J.C., Dahms, R.N., Lacaze, G., Manin, J., Pickett, L., 2012. Effects of pressure on fundamental physics of fuel injection in diesel engines. In: 12th International Conference on Liquid Atomization and Spray Systems (ICLASS). Heidelberg, Germany.

- Okong'o, N.A., Bellan, J., 2002. Direct numerical simulation of a transitional supercritical binary mixing layer: heptane and nitrogen. *J. Fluid Mech.* 464, 1–34.
- Oschwald, M., Smith, J., Branam, R., Hussong, J., Schik, A., Chehroudi, B., Talley, D.G., 2006. Injection of fluids into supercritical environments. *Combust. Sci. Technol.* 178 (1–3), 49–100.
- Pantano, C., Saurel, R., Schmitt, T., 2017. An oscillation free shock-capturing method for compressible van der Waals supercritical fluid flows. *J. Comput. Phys.* 335, 780–811.
- Peng, D.-Y., Robinson, D.B., 1976. A new two-constant equation of state. *Ind. Eng. Chem. Res.* 15 (1), 59–64.
- Petit, X., Ribert, G., Domingo, P., 2015. Framework for real-gas compressible reacting flows with tabulated thermochemistry. *J. Supercrit. Fluids* 101, 1–16.
- Petit, X., Ribert, G., Lartigue, G., Domingo, P., 2013. Large-eddy simulation of supercritical fluid injection. *J. Supercrit. Fluids* 84, 61–73.
- Pickett, L., Bruneaux, G., 2011. Engine Combustion Network. Combustion Research Facility, Sandia National Laboratories, Livermore, CA. (<http://www.sandia.gov/ECN>).
- Poling, B.E., Prausnitz, J.M., O'Connell, J.P., 2001. *The Properties of Gases and Liquids*. McGraw-Hill, New York.
- Qiu, L., Reitz, R., 2015. An investigation of thermodynamic states during high-pressure fuel injection using equilibrium thermodynamics. *Int. J. Multiphase Flow* 72, 24–38.
- Qiu, L., Wang, Y., Reitz, R.D., 2014. On regular and retrograde condensation in multiphase compressible flows. *Int. J. Multiphase Flow* 64, 85–96.
- Raju, M., Banuti, D.T., Ma, P.C., Ihme, M., 2017. Widom lines in binary mixtures of supercritical fluids. *Sci. Rep.* 7 (3027), 1–10.
- Roy, A., Joly, C., Segal, C., 2013. Disintegrating supercritical jets in a subcritical environment. *J. Fluid Mech.* 717, 193–202.
- Ruiz, A., 2012. Unsteady Numerical Simulations of Transcritical Turbulent Combustion in Liquid Rocket Engines. Institut Nationale Polytechnique de Toulouse Ph.D. thesis.
- Ruiz, A., Lacaze, G., Oefelein, J., Mari, R., Cuenot, B., Selle, L., Poinot, T., 2016. Numerical benchmark for high-Reynolds-number supercritical flows with large density gradients. *AIAA J.* 54 (6), 1445–1460.
- Saurel, R., Petitpas, F., Abgrall, R., 2008. Modelling phase transition in metastable liquids: application to cavitating and flashing flows. *J. Fluid Mech.* 607, 313–350.
- Schmitt, T., Selle, L., Ruiz, A., Cuenot, B., 2010. Large-eddy simulation of supercritical-pressure round jets. *AIAA J.* 48 (9), 2133–2144.
- Shyue, K.-M., 2001. A fluid-mixture type algorithm for compressible multicomponent flow with Mie-Grüneisen equation of state. *J. Comput. Phys.* 171 (2), 678–707.
- Sirignano, W., Delplanque, J.-P., 1999. Transcritical vaporization of liquid fuels and propellants. *J. Propul. Power* 15 (6), 896–902.
- Strang, G., 1968. On the construction and comparison of difference schemes. *SIAM J. Num. Anal.* 5 (3), 506–517.
- Takahashi, S., 1975. Preparation of a generalized chart for the diffusion coefficients of gases at high pressures. *J. Chem. Eng. Jpn.* 7 (6), 417–420.
- Terashima, H., Koshi, M., 2012. Approach for simulating gas-liquid-like flows under supercritical pressures using a high-order central differencing scheme. *J. Comput. Phys.* 231 (20), 6907–6923.
- Tian, L., Xu, Y., Kuerten, J.G.M., van der Vegt, J.J.W., 2016. An h-adaptive local discontinuous Galerkin method for the Navier-Stokes-Korteweg equations. *J. Comput. Phys.* 319, 242–265.
- Wang, X., Huo, H., Wang, Y., Yang, V., 2017. Comprehensive study of cryogenic fluid dynamics of swirl injectors at supercritical conditions. *AIAA J.* 55 (9), 3109–3119.
- Wood, A.B., 1930. *A Textbook of Sound*. G. Bell and Sons Ltd, London.
- Yang, V., 2000. Modeling of supercritical vaporization, mixing, and combustion processes in liquid-fueled propulsion systems. *Proc. Combust. Inst.* 28 (1), 925–942.
- Yang, V., Lin, N., Shuen, J., 1994. Vaporization of liquid oxygen (LOX) droplets in supercritical hydrogen environments. *Combust. Sci. Technol.* 97 (4–6), 247–270.
- Zong, N., Yang, V., 2008. Cryogenic fluid dynamics of pressure swirl injectors at supercritical conditions. *Phys. Fluids* 20 (5), 056103.